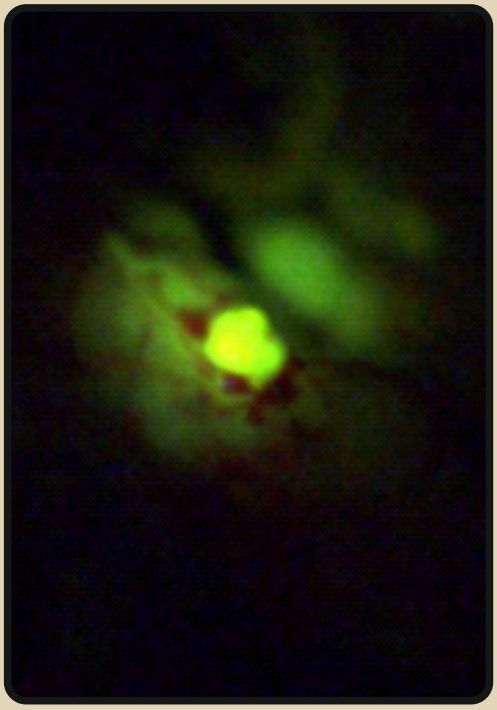
Volume 6, Issue 1, 2020

Journal of Biomedical Photonics & Engineering

Special Issue

"Laser and optical technologies in biomedicine and ecology"





Special Issue Editors:
Ivan A. Bratchenko and Aleksandra M. Mayorova

© 2020 J-BPE

 doi: 10.18287/JBPE20.06.010001

Journal of Biomedical Photonics & Engineering

by Samara National Research University

Volume 6, Issue 1 (March 2020)

Editorial Board

Editor-In-Chief

Valery V. Tuchin - Saratov National Research State University, Russian Federation;
Institute of Precision Mechanics and Control RAS, Russian Federation; a corr.-member of RAS

Deputy Editor-In-Chief

Valery P. Zakharov - Samara National Research University, Russian Federation

Editorial Board

Stefan Andersson-Engels (Tyndall National Institute, Ireland), **Alexey N. Bashkatov** (Saratov National Research State University, Russia), **Ekaterina Borisova** (Institute of Electronics, Bulgarian Academy of Sciences, Bulgaria), **Wei Chen** (University of Central Oklahoma, USA), **Arthur Chiou** (National Yang-Mind University, Taiwan), **Elina Genina** (Saratov National Research State University, Russia), **Min Gu** (Swinburne University, Australia), **Dror Fixler** (Bar-Ilan University, Ramat Gan, Israel), **Vyacheslav Kalchenko** (The Weizmann Institute of Science, Israel), **Nikolay G. Khlebtsov** (Institute of Biochemistry and Physiology of Plants and Microorganisms RAS, Russia), **Juergen Lademann** (Charite University Clinic, Germany), **Kirill V. Larin** (University of Houston, USA), **Martin Leahy** (University of Galway, Ireland), **Qingming Luo** (Hainan University, China), **Stephen J. Matcher** (University of Sheffield, Great Britain), **Aleksandra M. Mayorova** (Samara Branch of P.N. Lebedev Physical Institute of Russian Academy of Sciences, Russia), **Igor Meglinski** (University of Oulu, Finland), **Vladimir S. Pavelyev** (Image Processing Systems Institute RAS, Russia), **Francesco Pavone** (University of Florence, Italy), **Roberto Pini** (Institute of Applied Physics, Italy), **Igor A. Platonov** (Samara National Research University, Russia), **Juergen Popp** (Institute of Photonic Technology, Germany), **Alexander V. Priezzhev** (Moscow State University, Russia), **David Sampson** (The University of Western Australia, Australia), **Alexander Savitsky** (Institute of Biochemistry RAS, Russia), **Alexander P. Shkurinov** (Moscow State University, Russia, a corr.-member of RAS), **Peter So** (Massachusetts Institute of Technologies, USA), **Janis Spigulis** (University of Latvia, Latvia), **Ilya V. Turchin** (Institute of Applied Physics RAS, Russia), **Lihong V. Wang** (California Institute of Technology, USA), **Ruikang Wang** (University of Washington, USA), **Xunbin Wei** (Shanghai Jiao Tong University, China), **Dan Zhu** (Britton Chance Center for Biomedical Photonics, Huazhong University of Science and Technology, China).

Postal address:
39B Lukacheva st., room #301
Samara 443086, Russian Federation

 © 2020 J-BPE

doi: 10.18287/JBPE20.06.010001

Special Issue
“Laser and optical technologies in biomedicine and ecology”

Special Issue Editors

Ivan A. Bratchenko
Samara National Research University

Aleksandra M. Mayorova
Samara Branch of P.N. Lebedev Physical Institute of Russian Academy of Sciences

Used Figure from this issue on the Cover

Valery Shupletsov et al. Fluorescence Imaging System for Biological Tissues Diagnosis: Phantom and Animal Studies, 010303, Fig. 4 and 5 (adapted).

© 2020 J-BPE

Contents

Introduction

Foreword to the Special Issue on Laser and optical technologies in biomedicine and ecology 010101

Articles

Influence of Laser Activating Nutrient Media on Bacterial Growing Dynamics 010301
Lubov A. Kokorina, Anna V. Neupokoeva, Elena R. Gerok, and Ksenia V. Rogova

Study of Laser Radiation Effect on the Cornea of the Eye by Speckle Interferometry 010302
Victoria A. Fedulova, Aleksei V. Yuzhakov, and Olga I. Baum

Fluorescence Imaging System for Biological Tissues Diagnosis: Phantom and Animal Studies 010303
Valery Shupletsov, Ksenia Kandurova, Viktor Dremin, Elena Potapova, Mikhail Apanaykin, Ulyana Legchenko, and Andrey Dunaev

Practical implementation analysis of the fractal dimension calculating algorithm for the medical images by the example of neutrophil nuclei 010304
Semen A. Naydenov, Pavel A. Naydenov, and Elena V. Shevchenko

Solid-phase luminescence of pyrene in chitosan adsorbents 010305
Danila A. Tatarinov, Sofia R. Sokolnikova, and Natalia A. Myslitskaya

Electrical Properties of Porous Silicon as a Biosensor Material 010306
Kristina A. Ganichkina and Natalia V. Latukhina

Studies of Red Blood Cell Aggregation and Blood Oxygenation on the Basis of the Optoacoustic Effect in Biological Media 010307
Denis A. Kravchuk and Ksenia A. Voronina

 © 2020 J-BPE

 doi: 10.18287/JBPE20.06.010101

Foreword to the Special Issue on Laser and optical technologies in biomedicine and ecology

Dear Colleagues,

Once again, it is our pleasure to present you the Special Issue of the Journal of Biomedical Photonics & Engineering (J-BPE) with selected papers of the Biophotonics Workshop of the XVII All-Russian Youth Conference-Contest on Optics and Laser Physics (Samara, November 12-16, 2019). The conference-contest was organized by P.N. Lebedev Physical Institute (Samara Branch) and Samara National Research University and supported by Administration of Samara Region and Samara SPIE Student Chapter.

The Biophotonics Workshop gathers researchers scientific and educational institutions, and provides a platform for discussion of wide range questions including optical applications in medicine, biology, and ecology. The Biophotonics Workshop 2019 included the invited lectures of Prof. O. Baum (Federal Research Center "Crystallography and Photonics" of the Russian Academy of Sciences, Moscow, Russia) and Prof. E. Borisova (Institute of Electronics of the Bulgarian Academy of Sciences, Sofia, Bulgaria), invited reports of young scientists from FRC "Crystallography and Photonics" of RAS Yu. Alexandrovskaya and E. Kasianenko as well as contest reports of undergraduate and graduate students. Young researchers from Samara, Moscow, Kaliningrad, Nizhniy Novgorod, Orel, Saratov, Taganrog, and Irkutsk participated in the Biophotonics workshop this year.

The papers presented in the Special Issue of J-BPE cover a wide range of laser and optics modalities for biomedical and ecological purposes.

Lubov Kokorina *et al.* from Irkutsk State Medical University studied laser irradiation effect of nutrient media solutions on their microstructure and, as a result, a dynamics of bacterial growth in photomodified media. The authors experimentally showed that the growth rate of bacteria varies depending on the irradiation media time, that allows controlling the dynamics of bacterial cultures.

Victoria Fedulova *et al.* (Federal Research Center "Crystallography and Photonics" of the Russian Academy of Sciences) were engaged in studying of in essence new type of correction, which based on a modification of structure and a field of mechanical tension of a cornea. In their study, possibility of using a speckle interferometry method as a basis for the tracking system of cornea structural changes at thermal influence of a nondestructive laser radiation is considered. The authors also carried out the experiments that allowed them to proposed the polyacrylamide hydrogel composition with the temperature profile similar to the temperature profile of the cornea.

Valery Shupletsov *et al.* (Orel State University, Aston Institute of Photonic Technologies) describes the development of a fluorescence imaging system to define tumor surgical resection margins of abdominal organs. The authors proposed a low-cost optical tissue-mimicking phantom for quick calibration of fluorescence imaging systems depending on the target endogenous fluorophores. The capability of the developed fluorescence imaging system to register changes in

 doi: 10.18287/JBPE20.06.010101

fluorescence due to carcinogenesis was shown on two series of experimental measurements. The first part included measurements of the optical phantom with riboflavin mononucleotide (imitating flavin adenine dinucleotide) and protoporphyrin IX and the second part of the study included *in vivo* measurements of liver tumors modeled in mice.

Semen Naidenov *et al.* from Irkutsk State Medical University and Irkutsk State University presents the results of estimating a fractal dimension of neutrophil nuclei to determine their functional state. Calculations were carried out by a specially developed algorithm. The study has shown that the fractal theory can be applied to automate medical image processing.

Danila Tatarinov *et al.* (Kaliningrad State Technical University) highlights a preparation method of modified chitosan films for adsorption of pyrene from solution. Solid-phase luminescence of samples was studied, degree of extraction and index of polarity of microenvironment of pyrene molecules was determined. The authors proven possible to carry out luminescent analysis of substances for pyrene content using proposed films.

Kristina Ganichkina and **Natalia Latukhina** (Samara National Research University) presented a study directed on improving methods for analyzing blood glucose levels. The authors estimated the electrical properties of porous silicon nanocomposites with various glucose solutions. In particular, the current-voltage characteristics of glucose solutions in water and tear fluid, as well as porous silicon samples of various porosities saturated with these solutions were measured. The experiments demonstrated the capability of porous silicon as a promising material for creating an electric or combined optical-electric glucose biosensor.

Denis Kravchuk and **Ksenia Voronina** (Southern Federal University) proposed models of the processes of oxygen saturation and red blood cells (RBCs) aggregation in the blood. Models of oxygenated RBCs and their distribution in the blood were constructed using the Monte Carlo technique. The acoustic signals from oxygenated and deoxygenated RBCs were simulated at various levels of oxygen saturation. The authors found that the level of spectral power density of the acoustic signal varies significantly and allows one to estimate the percentage of oxygen saturation of red blood cells in the blood with implementation of optoacoustic method.

The highlighted papers of the Special Issue demonstrate potential of optical and laser technologies in modern medical and biological applications.

Special Issue Editors:

Ivan A. Bratchenko
Samara National Research University
E-mail: iabratchenko@gmail.com

Aleksandra M. Mayorova
Samara Branch of P.N. Lebedev Physical Institute of Russian Academy of Sciences
E-mail: mayorovaal@gmail.com

Influence of Laser Activating Nutrient Media on Bacterial Growing Dynamics

Lubov A. Kokorina, Anna V. Neupokoeva*, Elena R. Gerok, and Ksenia V. Rogova
Irkutsk State Medical University, Department of Microbiology, Virology and Immunology, Department of Medical and Biological physics, 1 Krasnogo Vosstaniya str., Irkutsk 664009, Russian Federation

*** e-mail:** annett_2005@inbox.ru

Abstract. The laser irradiation effect of nutrient media solutions on their microstructure and, as a result, on the dynamics of bacterial growth in photomodified media is considered in the article. It is experimentally shown that the growth rate of bacteria varies depending on the irradiation media time, that allows us to control the dynamics of bacterial cultures. © 2020 Journal of Biomedical Photonics & Engineering.

Keywords: laser biostimulation; structure modification.

Paper #3347 received 16 Jan 2020; revised manuscript received 17 Feb 2020; accepted for publication 7 Mar 2019; published online 12 Mar 2020. doi: 10.18287/JBPE20.06.010301.

1 Introduction

Laser radiation is widely used to modify a structure and properties of biomaterials, drugs, and biological fluids [1–4]. In the case of exposure to a liquid media, the energy of laser radiation is used to modify a microstructure of the liquid. It is known [5, 6] that organic molecules (for example, proteins macromolecules) and water molecules themself form clusters using hydrogen bonds. The larger size of such associate means the higher ratio of its mass to the surface and, hence, the smaller reactivity. It is shown [4, 7] that under the influence of laser radiation clusters of organic molecules can break up into smaller formations, because coherent monochromatic laser radiation causes intense movements of charged sections of macromolecules. As a result, the molecules break out of the clusters, creating more homogeneous mixture with fewer inhomogeneities.

On the other hand, the control of bacterial cultures growth is an urgent problem in medicine, because traditional methods of bacterial reproduction suppressing, for example, with the help of antibiotics, are not always effective. Therefore, some strains of Staphylococcus aureus have become resistant to a wide range of antibiotics, in particular to penicillins (methicillin, dicloxacillin, nafcillin, oxacillin, etc.) and cephalosporins. Resistance of bacteria leads to various complications after staphylococcal infection and causes high mortality. Therefore, the search for new methods for control of the bacterial growth dynamics is an urgent task.

The dynamics of bacterial culture development depends to a significant extent on both the presence of nutrients and their bioavailability. Therefore, there are three stages of cultivation for any bacterial culture in an *in vitro* closed environment: rapid growth under nutrients excess, “plateau” – the period when the processes of reproduction and death balance each other, and the decline period, when the depletion of nutrients leads to the predominance of the death processes over the growth processes of the culture. It is known that liquid or gel protein solutions are often used as a nutrient medium for the microorganisms cultivation [8], for example, meat-peptone agar. As noted above, dissolved substances form clusters (associates) in liquids by combining molecules. The associate size affects its diffusion through the bacterial membrane and, thus, its bioavailability as a food for bacterial cells. Therefore, the destruction of the molecule clusters, for example, under the influence of laser radiation, would allow us to change their suitability for assimilation by microorganisms.

The aim of this work is to determinate the effect of modification of the nutrient medium by laser irradiation on the growth dynamics of microorganisms in a closed system.

2 Materials and methods

The influence of nutrient medium laser exposure on the bacterial growth dynamics was evaluated. As a test model, we used a reference culture of Staphylococcus aureus (St. aureus) that was grown in a liquid medium (nutrient broth is an aqueous solution of peptone, fish meal hydrolysate, and sodium chloride). In the control cases, a microbial suspension was added to the liquid nutrient medium immediately after its preparation. In

experimental samples, the nutrient medium that is necessary for the development of bacterial culture was exposed to laser radiation in the green region of the spectrum (wavelength 532 nm, power 100 mW). The choice of this wavelength is determined by the results of previous experiments on the effect of laser radiation on protein solutions [9]. Laser radiation with wavelength of 532 nm, even under small exposure times, provides a larger change of the structure compared to the wavelength of 650 nm.

The irradiation of the nutrient medium was carried out in the "light boiler" mode. Laser radiation was directed from above to the liquid nutrient medium in a test tube, which was wrapped with a reflective layer. Thus, the liquid medium was affected not by direct radiation only, but also by reflected radiation. Laser radiation was exposed during 30, 60, and 120 sec (the total irradiation energy is 3 J, 6 J, and 12 J, respectively). After that, a microbial suspension was placed in the nutrient medium. It should be noted that the laser radiation affected the nutrient medium only and did not interact with bacteria. Every 12–24 hours during the week, a drop of liquid medium with microbial suspension was taken and seeded on a solid agar-based medium in four repetitions (4 Petri dishes). Further, the primary growth time was taken into account, the number of colony-forming units (CFU) was calculated and their types were described. Thus, for each of the 8 time points, 4 seeding procedures were carried out, a total of 32 samples for each series of experiments, or 128 samples in total. The average value and measurement error were calculated from 4 measurements for each time point.

3 Results

The first growth of bacteria in the control and experimental groups was recorded 12 hours after sowing (Fig. 1). However, in a group with nutrient medium irradiated during 120 sec growth was delayed: growth was observed only in one Petri dish.

There is a 24-hour active growth stage in the control group, where St. aureus was cultured in a non-laser-exposed medium (Fig. 1). At the same time, the number of bacteria has its maximum – 7.925 ± 0.15 lg CFU/ml. The number of cells decreases to 4.535 ± 0.11 lg CFU/ml from 24 hours point to the end of the experiment.

For the culture medium irradiated for 30 and 60 sec, the dynamics of the bacteria growth is identical to the control group in the first 24 hours. However, the medium irradiated for 30 sec later shows a smoother decrease of the colonies number that is 1.32 times greater at the end of experiment than for the non-irradiated medium. The difference significantly exceeds the error of the experiment at this stage.

The irradiation of the media during 60 sec increases the active breeding period of the microbial population to 72 hours. In addition, the population size reached its maximum value in comparison with all experimental cases (7.75 ± 0.5 lg CFU/ml). After that, the death processes began to predominate over the division processes (it is associated with the nutrient substrate depletion) and the number of bacteria decreased to 5.175 ± 0.35 lg CFU/ml, that differs from the control value within the experimental error.

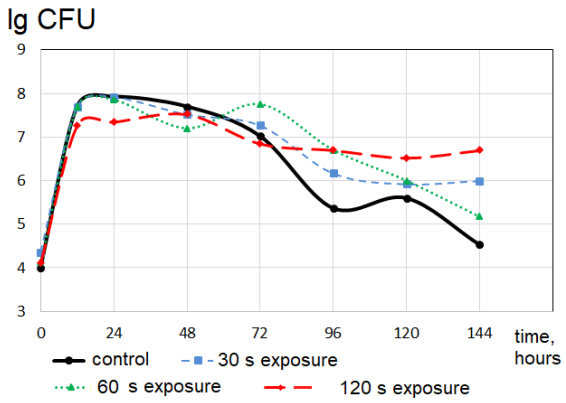


Fig. 1 The dependence of bacterial growth over the time (the abscissa axis sets time, the ordinate axis sets the logarithm of colony-forming units (CFU).

With an increase of the laser exposure time to 120 sec the bacteria growth was slowed down at the initial stage compared to the control group. In this case, the active breeding phase of the microbial population was extended to 48 hours, followed by a slight decrease in the number of colonies. "Plateau" is registered until the completing experiment, so the processes of reproduction and death are approximately at the same level. It should be noted that the absence of bacteria amount reducing phase leads to the fact that the amount of colonies in the 120 sec exposure media exceeds the control value by 1.5 times to the end of the experiment.

The observed significant difference in growth dynamics is probably due to changes in the structure of the macromolecular clusters in the nutrient medium. Thus, at short exposure times (30 and 60 sec) the laser radiation energy is spent on increase of the cluster components mobility that leads to its disintegration into smaller formations and increase of the nutrients bioavailability in the solution. These changes cause an elongation of the bacteria growth phase and a sharp depletion of nutritional resources, that later leads to intensive bacterial death.

Under irradiating the nutrient medium during 120 sec, we observe the opposite effect: at the initial stage, the bacteria growth rate was less than control, and this fact indicates a decrease of the nutrients bioavailability. We offer two explanations for this phenomenon. First, under the excess of the laser radiation energy, additional energy is enough not only to destroy clusters but also to change the secondary and tertiary conformation of protein molecules that negatively affects their interaction with receptors on the bacterial membrane. Second, the explanation may be since according to some experimental data [10] laser radiation causes an increase in the homogeneity of the

liquid media structure, i.e., there are two parallel processes: division of the large clusters into smaller ones, and on the contrary, fusion, enlargement of the smallest clusters. Thus, the dispersion degree of the clusters size decreases, while the percentage of the smallest ones decreases, which also causes a bacteria growth slowdown in the media and increases the time until the resources are depleted, that looks like a long "plateau" on the graph.

4 Conclusion

Thus, it is experimentally established that laser irradiation with a wavelength of 532 nm significantly affects growth dynamics of the Staphylococcus aureus in a closed system. Nutrient media irradiated for 30 and 60 sec contribute to a longer growth period compared to the control that is probably associated with decrease in the characteristic size of clusters formed by macromolecules of nutrients that increases their bioavailability. Irradiation of the nutrient medium during 120 sec leads to the opposite effect: the rate of the bacteria growth slows down, the consumption of the nutrient resources decreases, and the phase of active death does not occur by the end of the observation time.

Disclosures

All authors declare that there is no conflict of interests in this paper.

References

1. G. E. Brill, A. V. Egorova, I. O. Bugaeva, and G. V. Ponomarev, "Laser modification of the dehydration self-organization of the dimegin hydrophilic photosensitizer," Laser medicine 15(2), 59–60 (2011) [in Russian].
2. S. Kudryashov, Yu. Kolobov, and A. Ligachev, "Multiscale femtosecond laser texturing and chemical modification of the surface of medical titanium implants," Photonics 3(45), 14–22 (2014) [in Russian].
3. T. I. Karu, V. I. Yusupov, V. N. Bagratashvili, A. L. Drozdov, and V. M. Chudnovskii, "Influence of low-intensity red diode and laser radiation on the locomotor activity of sea urchin sperm," Doklady Biochemistry and Biophysics 457(1), 146–148 (2014).
4. A. N. Malov, A. Yu. Seteikin, A. V. Neupokoeva, E. S. Musatova, I. E. Golub, L. V. Sorokina, V. S. Fetschenko, and A. A. Vaichas, "The laser radiation action on the biological objects," Optik 124(23), 6034–6041 (2013).
5. E. A. Manykin, V. B. Oshurko, "Water ordering under laser radiation," Laser Physics 17(6), 842–852 (2007).
6. V. D. Lakhno, Clusters in Physics, Chemistry, Biology, NITs "Regular and chaotic dynamics", Izhevsk, Russia (2001) [in Russian].
7. A. N. Malov, A. A. Vaichas, Laser Control of Biomineral Formation. Physical Principles and Prospects of Developing New Medical Nanotechnology, Palmarium Academic Publishing, Saarbrucken, Deutschland (2016) [in Russian]. ISBN 978-3-659-60476-8.
8. N. V. Prozorkina, L. A. Rubashkina, Fundamentals of Microbiology, Virology and immunology, Phoenix, Rostov na Donu, Russia Federation (2002) [in Russian]. ISBN 5-222-02499-7.
9. A. N. Malov, S. A. Nebogin, A. V. Neupokoeva, and A. A. Vaychas, "Probe microscopy of biological fluid crystallograms after laser impact," Journal of Biomedical Photonics & Engineering 4(1), 010405 (2018).
10. A. V. Neupokoeva, E. A. Kuzina, N. S. Moskalev, A. I. Nikonova, and S. A. Nebogin, "Laser photomodification of insulin solution," Journal of Biomedical Photonics & Engineering 5(2), 20301 (2019).

Study of Laser Radiation Effect on the Cornea of the Eye by Speckle Interferometry

Victoria A. Fedulova, Aleksei V. Yuzhakov, and Olga I. Baum*
Federal Research Center "Crystallography and Photonics" of the Russian Academy of Sciences, 59 Leninskiy prospect, Moscow 119333, Russian Federation

*** e-mail:** baumolga@gmail.com

Abstract. The existing techniques of laser vision correction – one of the most widespread operations – are based presently on a surgical intervention in cornea tissue. Our science team is engaged in studying of in essence new type of correction based on a modification of structure and the field of mechanical tension of a cornea. In this work, the possibility to use of a speckle interferometry method as a basis for the tracking system of cornea structural changes at thermal influence of a nondestructive laser radiation is considered. Also for a cornea, the polymeric phantom was picked up. © 2020 Journal of Biomedical Photonics & Engineering.

Keywords: cornea; speckle interferometry method; polymeric phantom.

Paper #3350 received 30 Jan 2020; revised manuscript received 10 Mar 2020; accepted for publication 10 Mar 2020; published online 20 Mar 2020. doi: 10.18287/JBPE20.06.010302.

1 Introduction

The invention of lasers was a huge step forward for many fields of science. In medicine, lasers have become an important tool in oncology, dentistry, dermatology, surgery, and other fields. Currently, lasers have become very widespread in ophthalmology. According to the journal "Ophthalmology", about 2 billion people suffer from myopia and this number will reach about 5 billion by 2050 [1]. In addition, serious concern is caused by the fact that problems with the visual system arise at an increasingly young age. So, among first graders, about 5% of children suffer from myopia, by the end of school this number increases to 25–30%, which contributes to the growing demand for vision correction.

Refractive surgery is based on changing the shape of the cornea – the anterior, most convex transparent part of the eyeball, one of the main refractor of the eye. It was previously believed that the cornea consists of 5 layers: the epithelium, the anterior border (Bowman) membrane, the stroma, the posterior border membrane (Desmetamen membrane) and the posterior epithelium (endothelium) [2]. However, in 2013, the sixth layer was discovered, which was called the Dua layer [3].

Now, changing the shape of the cornea is done by correcting the shape of the stroma that does not have the ability to regenerate. Different methods differ in various approaches to overcoming the epithelium and the Bowman membrane that can be restored after damage. Currently, several types of correction are distinguished: PRK (photorefractive keratectomy), LASIK (Laser-Assisted in Situ Keratomileusis), LASEK (laser subepithelialkeratomileusis) [4], ReLEx SMILE [5].

The classical PRK method is as follows: after local anesthesia, de-epithelization is performed (mechanically, laser, or in another way), then the refraction stage itself is carried out (laser operation in the stroma), and, if necessary, the installation of protective lenses. Currently, a variant of photorefractive keratectomy, called trans-PRK, is a one-step technique that uses the cold ablation technique using an excimer laser.

PRK was recognized as the optimal method for the correction of mild and moderate myopia, however, with a high degree of myopia and astigmatism, the likelihood of postoperative complications and under correction is quite high. Besides, a sufficiently long recovery period causes certain inconveniences, as a result of which attempts to find another way of correction were not abandoned. LASIK was introduced in 1989. This type of correction allows you to work in deeper stroma layers. The innovation of LASIK consists in the formation of a corneal flap from the epithelial layers in the form of a circle connected to the rest of the cornea "leg" with a thickness of about 150 microns. Then the corneal flap rises and is laid aside to open the stromal zone of the cornea, on which the refractive stage of the operation itself is carried out. After changing the profile of the stroma, the epithelial flap returns to its place.

Modern vision correction technologies imply not only proper improvement of acuity and accommodation, but also an improvement in the quality of vision, as well as minimizing discomfort during and after surgery. A group of German ophthalmologists have developed the ReLEx method – Refractive Lenticule Extraction. At the moment, ReLEx SMILE is the only intrastromal corneal refractive laser operation performed without cutting out the surface corneal flap. The essence of the method is as follows: after local anesthesia, a lenticule is formed intrastromically, after that a small incision is made (from 2 to 4 mm). The lenticule is separated from the rest of the stroma by special tools, and then removed through the incision. The final step is washing the corneal pocket.

Due to the relatively recent introduction into practice, objective statistics for long-term follow-up of patients undergoing ReLEx SMILE do not yet exist, however, clinical data convincingly support this type of correction. The risk of postoperative complications is much lower than with other types of correction. It is obviously due to the smaller size of the dissection of biological tissue. In connection with these observations, it was concluded that it is necessary to introduce into the clinic a technique that does not violate the integrity of the biological tissues of the eye.

Our scientific group is studying a fundamentally new approach to the correction of refraction, based on the modification of cornea and sclera structure and their mechanical stresses field. The method consists of a combination of orthokeratology with laser radiation that does not damage the integrity of the eye tissue [6, 7]. Using a laser helps changing the conformation of collagen molecules located on the periphery of the cornea and in the limb. The method uses a special header that creates a circular distribution of the intensity of laser radiation [8–11], that allows us to achieve a more uniform effect of the weakening of mechanical stresses and leads to a reduction in laser-induced complications, since symmetric with respect to the paracentral zone cornea, but sequential irradiation of a number of points can lead to asymmetry of the corneal tension in the optical zone and the occurrence of astigmatism, keratoconus and other complications [8]. In addition, research is being carried out in the direction of developing a control system that allows one to determine the threshold for the onset of stress relaxation in the corneal tissues during laser irradiation. The studies are conducted in two different directions, one of which is based on optical coherent elastography [12–17], and the second direction is based on the speckle interferometry method, that the present work is devoted to.

2 MATERIALS AND METHODS

2.1 Eye tissue

The experiments were conducted *ex vivo* on pig eye samples. The extracted eyes were immediately frozen and stored at a temperature of −4 to 10 °C. In preparation for the experiment, the eyes were thawed in physiological saline for 30 minutes at room temperature. Immediately before the experiment, the samples were removed from physiological saline and slightly dried in air to avoid absorption by excess water on the surface, and then placed in a special holder. All experiments were repeated at least 5 times.

2.2 Polyacrylamide hydrogels

In the mid 80s of the XX century, the widespread use of synthetic polymer materials for medical purposes began. Polymers and polymeric materials are used in various fields, for example, as diagnostic and therapeutic drugs (long-acting drugs, protecting tissues surrounding tumor from radiation, physiologically active polymers), anti-burn surgery, suture and dressings. However, the greatest distribution of polymeric materials was in plastic and reconstructive surgery.

In this work, we used polyacrylamide hydrogels (PAAG), which include acrylamide, NN'-methylenebisacrylamide, ammonium persulfate and TEMED (tetramethylethylenediamine).

The structure of acrylamide is as follows: $CH_2 = CH – CONH_2$. NN'–methylenebisacrylamide (Bisacrylamide) – $(CH_2 = CH – CONH)_2 –CH_2 –$ acts as a “crosslinking” of linear acrylamide polymers. Ammonium persulfate is used to initiate the polymerization reaction (Fig. 1a). As a result of a homolytic rupture of the bond between oxygen atoms, two free radicals are formed (Fig. 1b) with a sufficiently long lifetime. The unpaired electron at the oxygen atom allows the radical to initiate the cleavage of the double bond in the acrylamide molecule and the formation of a new radical, in which the unpaired electron belongs to the carbon atom (Fig. 1c).

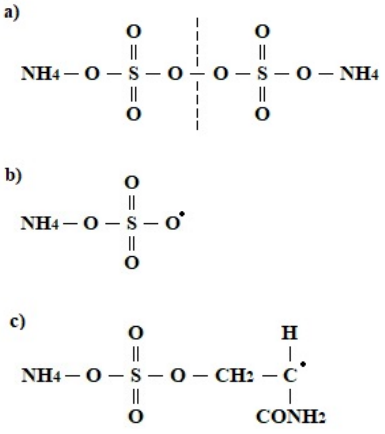


Fig. 1 The molecular structure of ammonium persulfate (a), free radical (b), and the combination of ammonium persulfate with acrylamide (c).

In turn, this radical is capable of causing a double bond in the next acrylamide molecule to break and to continue the polymerization chain reaction that ends

only after the two meets and the formation of the usual covalent bond.

One of the end groups of bisacrylamide can be integrated into the growing chain of a linear polymer. Its second end group may appear in another polymer chain, thus forming a crosslink – a bond between the polymer strands of acrylamide. The result of a large number of such bonds is a large branched network of hydrogel. TEMED is the catalyst for this process.

In this work, the main criteria for polyacrylamide hydrogels were the degree of crosslinking (determined by the ratio of acrylamide and bisacrylamide) and the percentage of the total mass of acrylamide and bisacrylamide to the volume of the solution. Based on the tabular data, a calculation was made for the intermediate values of these parameters. The necessary masses of substances included in the composition were measured on electronic scales, and then they were added to distilled water and mixed until completely dissolved. Then a catalyst (TEMED) was added to the solution and after that the hydrogel was collected in a syringe to give it a cylindrical shape convenient for research.

2.3 Speckle-Interferometry Method

Laser speckle-contrast technique (LSCI), due to its simplicity of execution, provides quick information on a wide area of motion of particles scattering light [18]. Over the past 15 years, it has become widely used as a tool for visualizing blood flow in the brain [19], skin [18], retina [20] and kidneys [21]. At the same time, the method itself continues to develop actively in terms of improving temporal and spatial resolutions, increasing the signal-to-noise ratio and searching for new applications [22–26].

The technique is based on the analysis of the speckle pattern arising as a result of random interference of coherent light scattered by a medium consisting of light-scattering particles. The motion of scattering particles leads to fluctuations in the interference pattern that can be recorded as changes in the intensity by the camera. Temporal and spatial statistics of the recorded speckle picture contains information about the movement. In particular, due to the finite integration time of the camera, motion will blur the speckle pattern, reducing speckle contrast.

The most common way to quantify blur is by calculating local speckle contrast [18, 19], that can be related to speed using autocorrelation functions of the field and intensity [19]. Theoretically, the contrast of a polarized speckle pattern takes values from 0 to 1 [27] (0 means that the scatters are fast enough to completely blur the speckle pattern, and 1 corresponds to a static, fully developed speckle pattern).

In this study, we used a LS-1.56 fiber laser (IPG Photonics Corp.) operating at a wavelength of 1.56 μm, with an output power of up to 5 W and the ability to control the duration of laser pulses and interpulse pauses. Irradiation mode: pulse-periodic mode, power density 15–56 W/cm^2, exposure time 15 s, pulse duration and the interval between pulses 500 and 300 ms, respectively. The radiation was supplied through an optical fiber with a diameter of 600 μm, directed at an angle of 15° to the normal surface. Simultaneously with heating, the sample was illuminated with a wide beam of a helium-neon laser with an incidence angle of 45°. The probe beam reflected normally to the sample is detected by a 2D camera (Videozavr, VZ-M50S, 1296 × 972 pixels, 21 frames/s) to obtain an image and to monitor changes in the statistical properties of speckle patterns caused by heating. The surface temperature was monitored using an IR camera FLIR A615.

The obtained images were used to calculate the statistical functions of speckle patterns, such as the average light intensity, contrast (autocorrelation function), Pearson's cross-correlation coefficient (decorrelation function).

The average value of the intensity was calculated by the equation:

$$<I_k>=\frac{1}{M*N}\sum_{m=1}^{M}\sum_{n=1}^{N}I_k, \quad (1)$$

where $<I_k>$ is the average intensity value for frame k, I_k is the intensity value at the point of frame k with coordinates $\{m, n\}$, M is the width of the frame in pixels, N is the height of the frame in pixels.

To calculate the contrast function, we used the following relation:

$$V_k=\frac{\sigma_{I_K}}{\langle I_k\rangle}=\frac{\sqrt{\langle I_k\rangle^2-\langle I_k^2\rangle}}{\langle I_k\rangle}, \quad (2)$$

where V_k is the value of the contrast function calculated for each frame k.

The Pearson cross-correlation coefficient was calculated using the following equation:

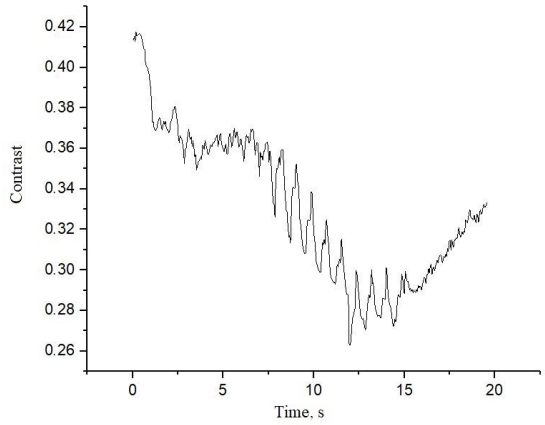
$$D_{k,l}=\frac{\operatorname{cov}\langle I_k, I_l\rangle}{\sigma_{I_k}\sigma_{I_l}}=\frac{\langle I_k I_l\rangle-\langle I_k\rangle\langle I_l\rangle}{\sqrt{\langle I_k\rangle^2-\langle I_k^2\rangle}\sqrt{\langle I_l\rangle^2-\langle I_l^2\rangle}}, \quad (3)$$

where $D_{k,l}$ is the value of the cross-correlation Pearson coefficient calculated for each pair of frames k and l.

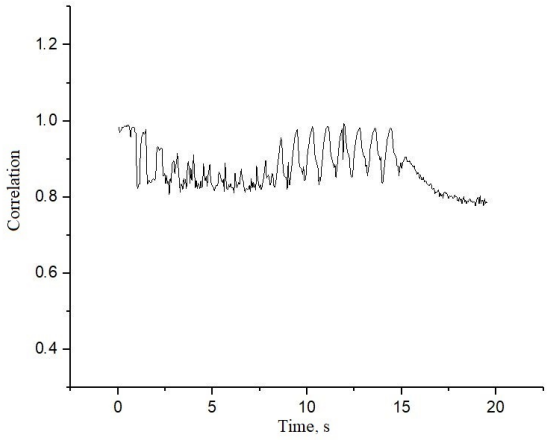
3 RESULTS AND DISCUSSION

The values of the contrast and correlation functions were measured for regions at the periphery and in the central part of the cornea for a pulse-periodic laser heating regime. On the graphs obtained, the denaturation moments are clearly visible, that can be determined by increasing the contrast graphs and by reducing the fluctuations of the correlation function. In the comparative graphs (Fig. 2), presenting the dependence of the contrast function and the correlation on time for the pulse-periodic mode, the motion of tissue inhomogeneities associated with its periodic

thermal expansion and contraction due to the laser operation mode is noted.



(a)

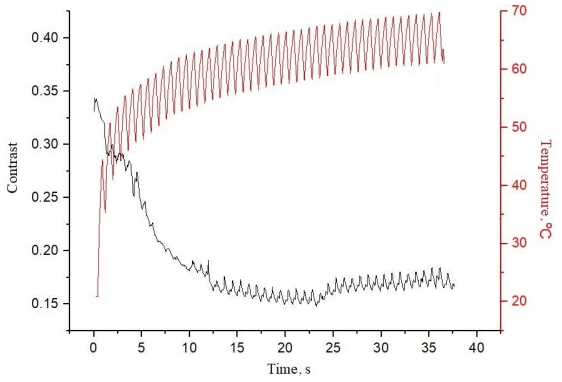


(b)

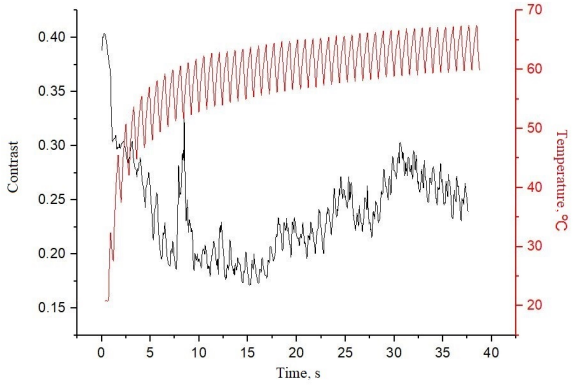
Fig. 2 Temporal dependences of contrast (a) and correlation coefficient (b) during heating of the cornea.

The oscillation amplitude of the contrast function for a region located in the central part of the cornea (Fig. 3a) is noticeably smaller compared to the oscillation amplitude for the periphery (Fig. 3b) that indicates a higher thermal resistance for central points. In the series of graphs obtained for the central part, the peaks of the contrast function are much less common than on the periphery, since when approaching the limb the stromal plates overlap each other that leads to the appearance of inhomogeneities associated with a violation of the parallelism of the collagen fibers.

Also graphs of the dependence of contrast on time were obtained for the regime that expects of stress relaxation. The biological tissue was irradiated for 20 sec (Fig. 4a), then it was soaked in saline for 5 min, and a 20 sec irradiation was repeated (Fig. 4b). The obtained graphs showed a qualitative similarity in the rate of decrease in the contrast function and the similarity of temperature profiles. The achieved maximum temperature also coincides, that allows us to conclude that the thermomechanical characteristics of the cornea are restored. The variability of the results of repeated experiments is within 10% while maintaining the qualitative shape of the curves that indicates the potential use of this method as a control system.



(a)

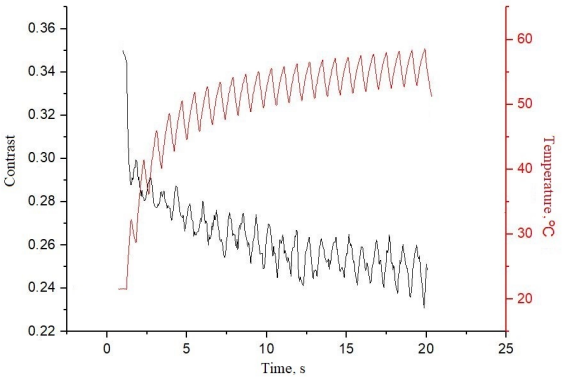


(b)

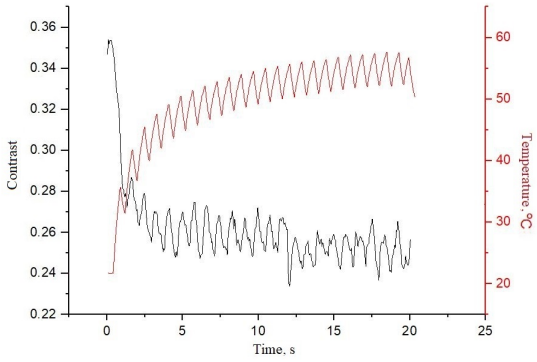
Fig. 3 Temporal dependences of contrast and temperature during pulse-periodic heating of the central (a) and peripheral (b) areas of the cornea.

A series of experiments was carried out for hydrogels with various degrees of crosslinking and the percentage of monomers in order to select a temperature profile that is most similar to the temperature profile obtained for the pig's cornea. The result of experiments series was the selection of the hydrogel composition with the temperature profile (Fig. 5a) similar to the temperature profile of the cornea. The composition of the obtained hydrogel includes Acrylamide – 0.2 g; Bisacrylamide – 0.0222 g; Ammonium persulfate – 0.0005 g; TEMED – 0.0001 g; Distilled water - 2 ml. The crosslinking degree of this hydrogel is 1:19, the percentage of monomers is 10%. At the same percentage of monomers, but with a lower degree of crosslinking (1:9), a noticeable similarity of temperature profiles is observed, but after about 25 sec of irradiation, the graphs begin to diverge (Fig. 5b). When the degree of crosslinking is 1:19 and the percentage of

monomers is 30%, the temperature profiles do not coincide.



(a)



(b)

Fig. 4 Temporal dependences of contrast and temperature during initial (a) and repeated (b) pulse-periodic heating of the cornea.

In the future, it will be used for the manufacture of phantoms for studies of thermal conductivity and the selection of optimal laser irradiation modes for various irradiation geometry.

4 Conclusion

In this work, a PAAG was selected with the temperature profile corresponded to the temperature profile of the cornea under pulse-periodic laser heating.

It was shown that the time and temperature dependences of the contrast and correlation functions make it possible to track the onset of structural changes in the corneal tissues during pulse-periodic laser heating. The difference in the behavior of these curves for the central and peripheral areas of the cornea is shown.

The obtained results and their repeatability allow us to conclude that it is possible to use the speckle interferometry method as a basis for a system for monitoring of the structural changes in the cornea associated with the thermal effect of laser radiation. The method requires further tuning to more clearly present the results of the experiment, but the qualitative similarity of the obtained graphs and the ability to track the moments of denaturation prove the feasibility of its development.

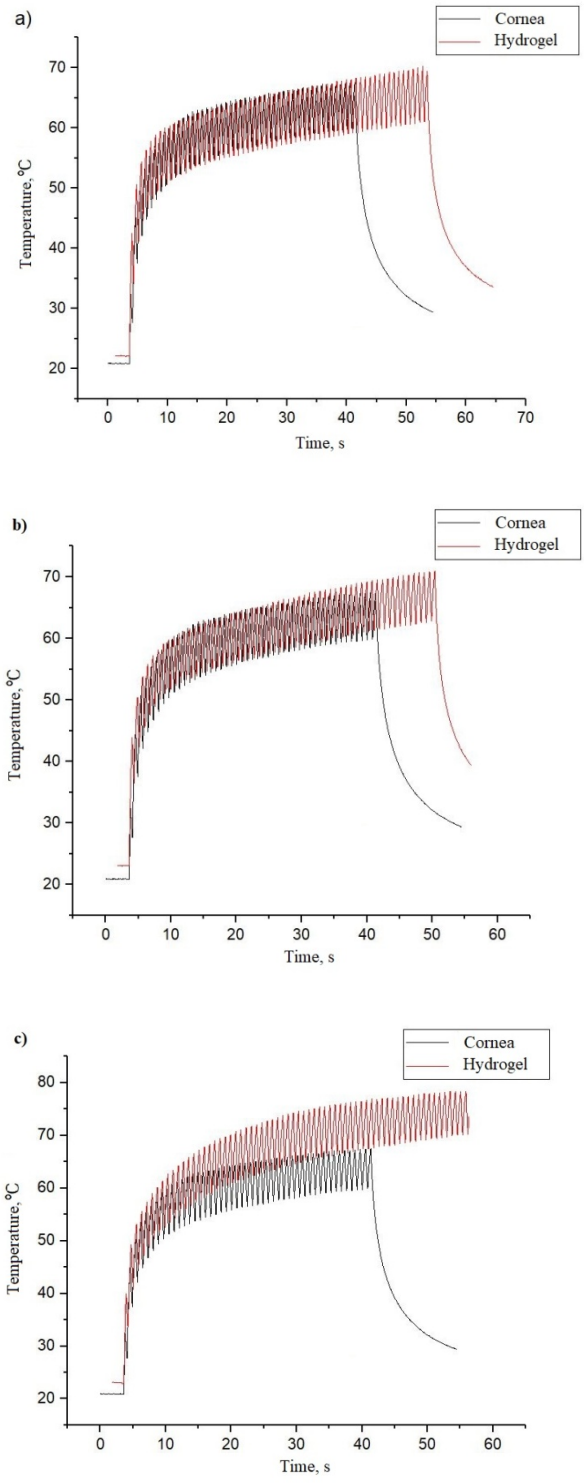


Fig. 5 Temperature profiles of the cornea and PAAG: a) the degree of crosslinking 1:19, the percentage of monomers 10%; b) the degree of crosslinking 1:9, the percentage of monomers 10%; c) the degree of crosslinking 1:19, the percentage of monomers 30%.

Disclosures

All authors declare that there is no conflict of interests in this paper.

Acknowledgments

This work was supported by the Ministry of Science and Higher Education of Russian Federation within the State assignment FSRC «Crystallography and Photonics» RAS.

References

1. B. A. Holden, T. R. Fricke, D. A. Wilson, M. Jong, K. S. Naidoo, P. Sankaridurg, T. Y. Wong, T. J. Naduvilath, and S. Resnikoff, "Global Prevalence of Myopia and High Myopia and Temporal Trends from 2000 through 2050," Ophthalmology 123(5), 1036–1042 (2016).
2. K. E. Johnson, Histology and cell biology, Williams & Wilkins, Baltimore, Maryland (1991).
3. H. S. Dua, L. A. Faraj, D. G. Said, T. Gray, and J. Lowe, "Human Corneal Anatomy Redefined," Ophthalmology 120(9), 1778–1785 (2013).
4. S. Taneri, J. D. Zieske, and D. T. Azar, "Evolution, techniques, clinical outcomes, and pathophysiology of LASEK: review of the literature," Survey of Ophthalmology 49(6), 576-602 (2004).
5. W. Sekundo, J. Gertnere, T. Bertelmann, and I. Solomatin, "One-year refractive results, contrast sensitivity, high-order aberrations and complications after myopic small-incision lenticule extraction (ReLExSMILE)," Graefe's Archive for Clinical and Experimental Ophthalmology 252(5), 837–843 (2014).
6. E. N. Sobol', O. I. Baum, A. V. Bol'shunov, V. I. Siplivy, N. Y. Ignat'eva, O. L. Zakharkina, V. V. Lunin, A. I. Omelchenko, V. A. Kamensky, and A. V. Mjakov, "Eye Tissue Structure and Refraction Variations upon Nondestructive Laser Action," Laser Physics 16(5), 735–740 (2006).
7. A. Bolshunov, E. Sobol, S. Avetisov, O. Baum, V. Siplivy, and A. Omelchenko, "A new method of the eye refraction correction under nonablative laser radiation," ActaOphthalmologica 89 (2011).
8. O. I. Baum, A. V. Yuzhakov, A. V. Bolshunov, V. I. Siplivyi, and O. V. Khomchik, "New laser technologies in ophthalmology for normalisation of intraocular pressure and correction of refraction," Quantum electronics 47(9), 860 (2017).
9. O. Baum, A. Yuzhakov, A. Omelchenko, A. Bolshunov, V. Siplivy, and E. Sobol, "Laser-assisted correction of eye cornea refraction with ring-shaped laser beam," Proceedings of SPIE 104170, 104170H (2017).
10. O. I. Baum, A. I. Omelchenko, E. M. Kasyanenko, R. V. Skidanov, and N. L. Kazanskij, "New biophotonics methods for improving efficiency and safety of laser modification of the fibrous tunic of the eye," Vestnik oftalmologii 134(5), 4–14 (2018).
11. O. I. Baum, A. I. Omel'chenko, E. M. Kasianenko, R. V. Skidanov, N. L. Kazanskiy, A. V. Bolshunov, S. E. Avetisov, and V. Y. Panchenko, "Control of laser-beam spatial distribution for correcting the shape and refraction of eye cornea," Quantum Electronics 50(1), 87 (2020).
12. O. I. Baum, V. Y. Zaitsev, A. V. Yuzhakov, A. P. Sviridov, M. L. Novikova, A. L. Matveyev, L. A. Matveev, A. A. Sovetsky, and E. N. Sobol, "Interplay of temperature, thermal ‐ stresses and strains in laser ‐ assisted modification of collagenous tissues: Speckle ‐ contrast and OCT ‐ based studies," Journal of Biophotonics 13(1), e201900199 (2019).
13. V. Y. Zaitsev, A. L. Matveyev, L. A. Matveev, G. V. Gelikonov, A. Vitkin, A. I. Omelchenko, O. I. Baum, D. V. Shabanov, A. A. Sovetsky, and E. N. Sobol, "Multiparameter thermo-mechanical OCT-based characterization of laser-induced cornea reshaping," Proceedings of SPIE 10067, 100670V (2017).
14. V. Y. Zaitsev, A. L. Matveyev, L. A. Matveev, G. V. Gelikonov, O. I. Baum, A. I. Omelchenko, D. V. Shabanov, A. A. Sovetsky, A. V. Yuzhakov, A. A. Fedorov, V. I. Siplivy, A. V. Bolshunov, and E. N. Sobol, "Revealing structural modifications in thermomechanical reshaping of collagenous tissues using optical coherence elastography," Journal of biophotonics 12 (3), e201800250 (2019).
15. V. Y. Zaitsev, L. A. Matveev, A. L. Matveyev, A. A. Sovetsky, D. V. Shabanov, S. Y. Ksenofontov, G. V. Gelikonov, O. I. Baum, A. I. Omelchenko, A. V. Yuzhakov, and E. N. Sobol, "Optimization of phase-resolved optical coherence elastography for highly-sensitive monitoring of slow-rate strains," Laser Physics Letters 1(6), 065601 (2019).
16. V. Y. Zaitsev, A. L. Matveyev, L. A. Matveev, G. V. Gelikonov, A. Vitkin, A. I. Omelchenko, O. I. Baum, D. V. Shabanov, A. A. Sovetsky, and E. N. Sobol, "Multiparameter thermo-mechanical OCT-based characterization of laser-induced cornea reshaping," Proceedings of SPIE 10067, 100670V (2017).
17. V. Y. Zaitsev, A. L. Matveyev, L. A. Matveev, G. V. Gelikonov, A. I. Omelchenko, D. V. Shabanov, A. A. Sovetsky, O. I. Baum, A. Vitkin, and E. N. Sobol, "Optical coherence elastography assesses tissue modifications in laser reshaping of cornea and cartilages," Proceedings of SPIE 10496, 104960C (2018).

18. D. Briers, D. D. Duncan, E. Hirst, S. J. Kirkpatrick, M. Larsson, W. Steenbergen, T. Stromberg, and O. B. Thompson, "Laser speckle contrast imaging: theoretical and practical limitations," Journal of Biomedical Optics 18(6), 066018 (2013).
19. D. A. Boas, A. K. Dunn, "Laser speckle contrast imaging in biomedical optics," Journal of Biomedical Optics 15(1), 011109 (2010).
20. A. Y. Neganova, D. D. Postnov, J. C. B. Jacobsen, and O. Sosnovtseva, "Laser speckle analysis of retinal vascular dynamics," Biomedical Optics Express 7(4), 1375–1384 (2016).
21. D. D. Postnov, N.-H. Holstein-Rathlou, and O. Sosnovtseva, "Laser speckle imaging of intra organ drug distribution," Biomedical Optics Express 6(12), 5055–5062 (2015).
22. A. S. Abdurashitov, V. V. Lychagov, O. A. Sindeeva, O. V. Semyachkina-Glushkovskaya, and V. V. Tuchin, "Histogram analysis of laser speckle contrast image for cerebral blood flow monitoring," Frontiers of Optoelectronics 8(2), 187–194 (2015).
23. D. D. Postnov, O. Sosnovtseva, and V. V. Tuchin, "Improved detectability of microcirculatory dynamics by laser speckle flowmetry," Journal of Biophotonics 8(10), 790-794 (2015).
24. D. D. Postnov, V. V. Tuchin, and O. Sosnovtseva, "Estimation of vessel diameter and blood flow dynamics from laser speckle images," Biomed.Optics Express 7(7), 2759–2768 (2016).
25. A. Abdurashitov, O. Bragina, O. Sindeeva, S. Sindeev, O. V. Semyachkina-Glushkovskaya, and V. V. Tuchin, "Off-axis holographic laser speckle contrast imaging of blood vessels in tissues," Journal of Biomedical Optics 22(9), 091514 (2017).
26. Z. Hajjarian, H. T. Nia, S. Ahn, A. J. Grodzinsky, R. K. Jain, and S. K. Nadkarni, "Laser speckle rheology for evaluating the viscoelastic properties of hydrogel scaffolds," Scientific Reports 6(1), 37949 (2016).
27. D. D. Duncan, S. J. Kirkpatrick, and R. K. Wang, "Statistics of local speckle contrast," Journal of the Optical Society of America A 25(1), 9–15 (2008).

Fluorescence Imaging System for Biological Tissues Diagnosis: Phantom and Animal Studies

Valery Shupletsov[1*], Ksenia Kandurova[1], Viktor Dremin[1,2], Elena Potapova[1], Mikhail Apanaykin[3], Ulyana Legchenko[3], and Andrey Dunaev[1]

[1] Research and Development Center of Biomedical Photonics, Orel State University, 95 Komsomolskaya st., Orel 302026, Russia

[2] Aston Institute of Photonic Technologies, Aston University, Aston Triangle, Birmingham B4 7ET, UK

[3] Department of Industrial Chemistry and Biotechnology, Orel State University, 95 Komsomolskaya st., Orel 302026, Russia

*** e-mail:** valery.shupletsov@bmecenter.ru

Abstract. Currently, optical biopsy is a promising area of diagnosing the state of tissues in real time during the surgical treatment of oncological diseases. The important part of this direction is the development of fluorescence imaging systems and ensuring the accuracy of the calibration of optical measurements. The article describes the development of fluorescence imaging system to define tumor surgical resection margins of abdominal organs. In this study, we proposed of low-cost optical tissue-mimicking phantom combining solid base and liquid part that suitable for quick calibration of fluorescence imaging systems depending on the target endogenous fluorophores. The results of two series of experimental measurements are described. The first measurements of the optical phantom with riboflavin mononucleotide (imitating flavin adenine dinucleotide) and protoporphyrin IX demonstrated the sensitivity of the developed device to proportionally changing concentrations of target fluorophores. The second part of the study included *in vivo* measurements of liver tumors modeled in mice. The obtained results showed the ability of the developed fluorescence imaging system to register changes in fluorescence due to carcinogenesis. © 2020 Journal of Biomedical Photonics & Engineering.

Keywords: optical phantom; optical biopsy; fluorescence imaging; fluorescence spectroscopy; riboflavin; gelatin; porphyrin; hepatocellular carcinoma.

Paper #3358 received 13 Mar 2020; accepted for publication 19 Mar 2020; published online 24 Mar 2020. doi: 10.18287/JBPE20.06.010303.

1 Introduction

According to the World Health Organization statistics, oncological diseases remains the second leading cause of in mortality worldwide [1]. Approximately 18.1 million new cases of cancer were detected in 2018 and 9.6 million deaths from cancer occurred. A significant percentage of incidence and mortality rates is occupied by malignant tumors and their metastases that develop in the abdominal and gastrointestinal organs (liver, pancreas, stomach, esophagus, colon, rectum, etc.). One of the causes leading to deterioration of prognosis in patients is the difficulties in accurate diagnosis of area and depth of malignant infiltration during the surgical treatment.

The leading method for treating many malignant tumors including abdominal and gastrointestinal ones is surgery [2–4]. The surgical treatment is aimed at safely removing as much of the tumor tissue without the necessity of additional surgery as possible. The main challenge surgeons face in this case is accurate definition of resection margins during the surgery. Detection and differentiation of intact and tumor tissue before and during surgical treatment is usually done by palpation and visual examination followed by intraoperative histopathological analysis of samples

taken from suspicious tissue sites. Visual inspection in white light and palpation are limited in sensitivity and subjectivity of visual and tactile sensations of the surgeon as it is hard to clearly distinguish the presence of the tumor tissue at the places of resection. A procedure express biopsy of each tissue sample takes about 20–25 min, which significantly increases the duration of the surgery and may pose risks to the patient. Moreover, the samples are usually taken randomly from several places of resection edge, which enhances the probability of a false negative result and can lead to cancer reversal in up to 19% of cases [5, 6]. In this regard, the problem of developing new diagnostic methods that allow the surgeon to receive additional diagnostic information on localization of malignant tissues in the resection margin in real time remains relevant direction of medical and biomedical engineering research.

Currently, one of the most promising and rapidly developing areas of real-time diagnostics for solving surgical treatment problems is a large number of optical methods often combined in the literature by the term "optical biopsy" [7–10]. These methods are aimed at providing the results comparable to data obtained by traditional methods without the requirement to acquire a tissue sample and spend considerable amount of time to perform the analysis. Optical biopsy includes spectroscopy and imaging techniques used to assess various parameters of morphology and metabolism of biological tissues *in vivo* [11, 12]. Additional diagnostic information can increase the effectiveness of surgical treatment of cancer in general and provide decision making support for organ preserving treatment.

One of the optical effects widely used to study metabolic activity is fluorescence. Fluorescence diagnostic methods are based on probing the tissue with monochromatic radiation of the near ultraviolet or visible range, exciting the fluorescence of endogenous or exogenous fluorophores and recording secondary emission for further analysis. Two most popular approaches – fluorescence spectroscopy (FS) and fluorescence imaging (FI) – demonstrate significant sensitivity to the presence of pathological changes in tissues, in particular malignant ones [13–15]. Extensive studies have been conducted in this direction for several decades to develop methodologies and devices for effective distinguishing of normal and tumor tissues in various human organs (lungs, breast, colon, cervix, etc.) [16–18].

Currently, a number of systems for fluorescence-guided surgery have already been clinically tested and implemented in the practice of surgeons. However, many of these systems involve the use of special fluorescent dyes for optical diagnostics in the near infrared range [19]. On the other hand, changes in autofluorescence caused by altered metabolic processes are also studied for the purpose of malignancies diagnosis [10, 20, 21].

It is known that cells undergo malignant transformations during carcinogenesis proceed which lead to morphological and biochemical changes detectable by fluorescence methods. The metabolic rate activity affects the content of certain fluorophores, such as nicotinamide adenine dinucleotide (NAD) and flavin adenine dinucleotide (FAD). These coenzymes are contained in the cytosol and mitochondria and are involved in reactions providing cells with energy, acting as electron donors and acceptors. These substances undergo oxidation and reduction reactions and reduced NAD (NADH) and oxidized FAD demonstrate the greatest contribution to tissue fluorescence. Maximum NADH fluorescence emits in blue light under 365 nm excitation, while FAD fluorescence emits in green light under 450 nm excitation [20]. Several clinical studies show that oncological processes affect such parameters as fluorescence intensity and redox ratio (FAD/NADH) [22]. Active proliferation in hypoxia forces tumor cells to switch to a glycolytic type of metabolism. These conditions lead to an increase in the concentration of NADH, change in redox ratio of FAD and NADH (FAD/NADH) [23–25]. Several clinical studies of FAD in tumors showed the changes in its fluorescence associated with oncological processes as well [26–28]. As FAD is involved in several metabolic reactions (tricarboxylic acid cycle, oxidative phosphorylation, acetyl coenzyme A synthesis, etc.) [29], the increase in FAD fluorescence can be explained by an increase in metabolic activity in abnormal tissues, which indicates tumor growth [30].

It is also reported that oncological processes cause abnormal increase of porphyrins accumulation, which indicates specific metabolic disorders of tumor cells [23, 31]. Porphyrin, namely protoporphyrin IX (PpIX), accumulates in tumors more actively [32–34], which is widely used in photodynamic therapy. Autofluorescence diagnostics of porphyrins has sufficient sensitivity to the presence of tumor sites as well [35].

Thus, the contribution of the listed fluorophores (NADH, FAD, porphyrins) to the spectra of endogenous fluorescence is closely dependent on the state of the tissue, which indicates the relevance of the development of methodologies and technical implementation for their registration and analysis.

While the FS and FI methods can be successfully used for the fluorescence contrasting at the selected wavelength of the emission [36], the fluorescence measurements of endogenous fluorophores in living tissues can be challenging due to the overlap of the emission spectra of different fluorophores. Moreover, biological tissues are heterogeneous complex structures containing various fluorophores in different concentrations and at different depths [37, 38]. In order to correctly interpret the experimental data in future clinical applications, it is necessary to determine the contribution of each component to the total signal. For this purpose, researchers usually perform test measurements using normal or pathologically altered tissues of laboratory animals or specially designed optical phantoms. While the studies in model animals are more close to real conditions of clinical *in vivo*

measurements, they are also more resource consuming and it is harder to imitate certain optical properties. Optical phantoms allow one to mimic the typical interaction of optical radiation with biological tissue with determined parameters of absorption, scattering, fluorescence, etc., which can be implemented both as test method at the stage of development and as the calibration method for future routine running in practice. The images of optical phantoms can be also used to improve resolution and quantification of uncorrected images using, for example, the deconvolution method [39].

Currently, researchers use several forms of optical phantoms in their studies in order to reach the versatility of properties mimicked, decrease the cost of the phantom and ensure the quality conform to the application goal. Most of the phantom spectroscopic studies available in literature are based on the development of liquid phantoms, which are used for modelling infinite or semi-infinite single layer media with absorption, scattering and fluorescence effects [40, 41]. For imitation of soft tissue-mimicking fluorescence gel-wax phantom based on mineral-oil material is known to be created [42].

The concept of a thin solid optical tissue phantom to maintain the required geometrical shape, thickness and inhomogeneity similar to multi-layered tissues is a challenging task. Various materials are used to create this phantoms, such as epoxy, polyester resin, or polyurethane material, which provide the photostability needed in long-term imaging applications [43–45]. Several scientific studies describe single-layer and two-layer solid gelatin phantoms fabricated for fluorescence studies, which are used to mimic normal and dysplasia tissue conditions [46, 47]. In this case, gelatin is used to imitate the fluorescence of collagen, as this protein is the main structural component of connective tissues.

Therefore, the aim of this work was the development of FI system and an optical tissue-mimicking phantom for its calibration as a preliminary stage of complex development of FI technology for detecting tumor margins during the surgery. As a target endogenous fluorophores for this study, FAD and PpIX were chosen. As simplicity and accessibility should play an important role in development and using of this technology, the main objective of this study was to assess the possibilities of development of low-cost phantom.

2 Materials and Methods

2.1 Experimental Setup

The scheme of the experimental home-built setup developed in this study is presented in Fig. 1.

The excitation channel included 455 nm LLS-455 LED source (Ocean Optics, USA) to excite the endogenous fluorescence. The radiation from the source was directed through a condenser and MF445-45 bandpass filter (Thorlabs, Inc. USA) to the object to cut a narrow band of excitation and minimize the effect of other tissue fluorophores. The diameter of the illuminated spot was adjusted with a collimator in the range from 1 to 3 cm. The image recording channel included FGL495 and FGL610 glass filters (Thorlabs, Inc. USA) with cut-off wavelengths of 495 nm and 610 nm to attenuate backscattered source radiation and pass the certain bands of fluorescence radiation to the detector. The images were recorded by 340M-USB fast frame rate monochrome scientific CCD camera (Thorlabs, Inc. USA). The camera's area of interest was 2.5 cm in diameter. The camera is controlled by the standard ThorCam software (Thorlabs, Inc. USA).

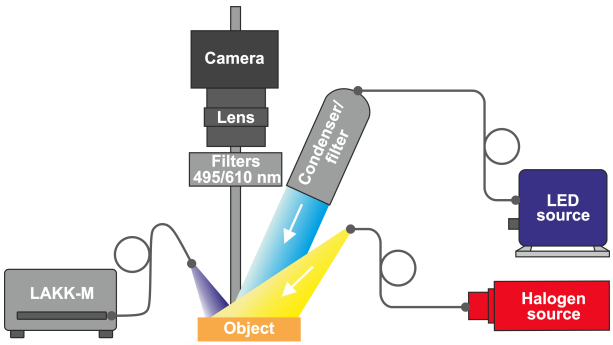


Fig. 1 The scheme of the experimental setup.

The FS method used for additional control measurements was implemented by the multifunctional laser diagnostic complex LAKK-M (SPE "LAZMA" Ltd, Russia). This device provided fluorescence excitation at 365 nm and 450 nm wavelengths and was equipped with 3 mm optical fiber probe (400 μm fibers, NA = 0.22). The spectra were recorded by the built-in spectrometer in the range of 340–800 nm.

In addition, the stabilized broadband radiation source of 360–2600 nm range SLS201L-M (Thorlabs Inc., USA) was used to record white light images and compare them with fluorescence images.

2.2 Tissue-mimicking Phantom Development

The idea of the optical phantom designed in this work was to combine the solid base for modeling of background collagen fluorescence and the liquid part to mimic the various concentrations of FAD and porphyrin fluorescence in biological tissues.

To produce optical phantoms imitating collagen fluorescence, it is possible to use gelatin, which is its hydrolyzed form. In this work, we created a multi-layer model consisting of sheets of gelatin with a thickness of less than 1 mm and a weight of less than 5 g. The optimal number of gelatin sheets was experimentally selected by comparing the fluorescence intensity levels of gelatin sheets and skin collagen. To simulate the FAD fluorescence spectrum, a 1% solution (26.6 μM/g) of riboflavin mononucleotide was used. This substance belongs to the flavin group and has the fluorescence spectrum similar to the spectrum of FAD. Riboflavin has a higher quantum yield, and, unlike FAD, its quantum yield within pH 4–8 does not depend on acidity [48]. It is known that the concentration of FAD

in human body usually varies from 0.1 to 1 μM/g [49]. In accordance with this data, four concentrations of riboflavin were selected close to the real concentrations of FAD in biological tissues. The solution of riboflavin mononucleotide was diluted with distilled water in the following ratios: 1:32, 1:64, 1:128 and 1:256. Thus, the solid base of the optical phantom was composed of two sheets of gelatin. The liquid part was made of the solutions of four different concentrations (0.84; 0.42; 0.21; 0.1 μM/g) of riboflavin distributed in four different areas of the phantom.

In our research, we used PpIX obtained chemically from the dark eggshell. It is known that PpIX, an immediate precursor of heme, is the main pigment that create the shell color [50]. Before the extraction, the eggshells were thoroughly washed of albumen and shell membranes and dried. 10 g of the eggshells were mixed with 150 ml of a 1 M hydrochloric acid solution. The reacting mixture was maintained until the release of carbon dioxide ceased. The undissolved residue was separated by filtration through a paper filter. The resulting emulsion was centrifuged to completely separate the layers. The top layer containing PpIX was transferred to a conical flask and 10 g of pre-calcined sodium sulfate was added to PpIX. The PpIX solution was separated from the salt by decantation and evaporated in a hot water bath until the solvent was completely removed. The residue was dissolved in 5 ml of dimethyl sulfoxide. As a result, PpIX was obtained at a concentration of 0.3 μM/g, which was applied to two sheets gelatin model similar to riboflavin.

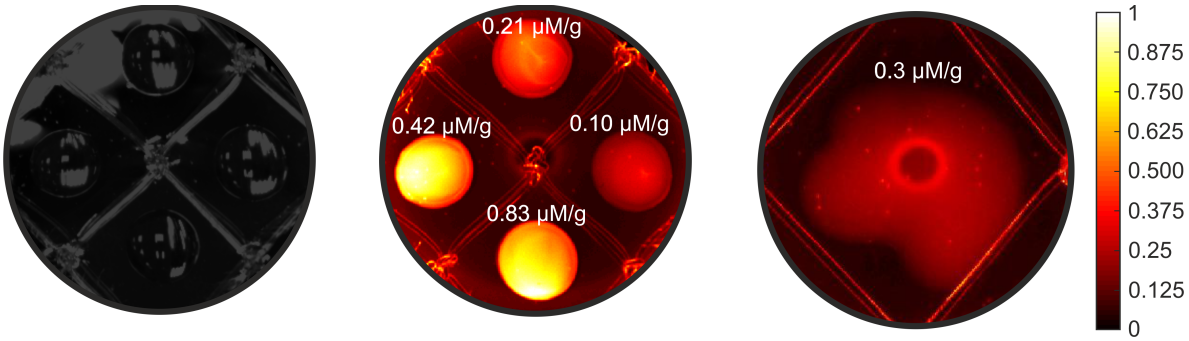
The research methodology included sequential registration of fluorescence images using the CCD camera and the spectrometer. Drops of the same volume (20 μl) with different concentrations of riboflavin or PpIX were applied to gelatin sheets using a micropipette. The resulting phantoms with riboflavin and PpIX were located on a non-fluorescent non-reflective surface. The registration of images was carried out in the following order. At the first stage, a 495 nm filter was installed in front of the camera, and fluorescence images were recorded 3 times. Then the image of phantoms in white light was recorded without a filter. At the second stage, the fluorescence spectra of each phantom were recorded 3 times. The results were processed on a personal computer using specially developed software in the Matlab environment.

2.3 Animals Model

The developed FI system demonstrated a rather high sensitivity to changes in the concentrations of dysplasia markers, such as flavins and porphyrins. In connection with this next step was also testing an animal model of liver cancer. The studies were approved by the Ethics Committee of Orel State University named after I.S. Turgenev (protocol No. 10 of 16.10.2017) and were carried out in accordance with the principles of Good Laboratory Practice [51]. Optical measurements were conducted in the BDF (C57Bl6xDBA) laboratory mice (male, n = 2, 20 weeks). H33 mouse hepatocellular carcinoma culture was previously implanted through a syringe into the medial lobe of the liver in a volume of 100 μl (50,000 cells/μl) per mouse during abdominal surgery. After approximately 2 months after the surgery, the experiments were carried out as mice increased their weight by more than 15% of the normal weight.

Before the measurements, the animal was anesthetized with Zoletil (Vibrac, France) in the standard dosage. The animal was fixed on a special platform in the back position. A transverse laparotomy was performed to gain access to the abdominal cavity. A surgeon performed a visual and palpatory examination of the abdominal cavity to determine the presence and localization of malignant and healthy tissue in the liver and other organs. The next step was to place the animal under the imaging channel of the experimental set up to adjust the focus, frame rate and exposure time according to the area of interest.

The research methodology included step-by-step registration of liver and tumor images in white light without filters and under 450 nm excitation with optical filters to obtain fluorescence images. The measurements were repeated 3 times. The obtained data was processed on a personal computer using custom developed software in the Matlab computing environment.



(a) (b) (c)

Fig. 2 Obtained images of the optical phantom: original image of riboflavin phantom in white light (a), fluorescence image of riboflavin phantom (b), fluorescence image of PpIX phantom (c).

3 Results and Discussion

3.1 Tissue-mimicking Phantom

As a result, the registered images of created optical phantom under halogen lamp illumination and LED illumination after preliminary processing are presented in Fig. 2a–c. The white light images (Fig. 2a) were recorded with exposure time of 20 ms, fluorescence images (Fig. 2b, c) were recorded with 400 ms exposure time. After that, the intensities were normalized to the maximum intensity to represent the obtained data in the range of [0; 1]. The fluorescence images of PpIX liquid on the gelatin surface of developed phantom was also recorded (Fig. 2c).

The intensity values of riboflavin and PpIX fluorescence were averaged in similar areas of each drop. The maximum fluorescence intensities obtained with the FS method were averaged and compared with the results of FI. Thereafter, the intensities were normalized by the maximum obtained value, so the maximum intensity was equal to 1. The results of fluorescence intensities measurements for each concentration of riboflavin and PpIX using FS modality are presented in Fig. 3.

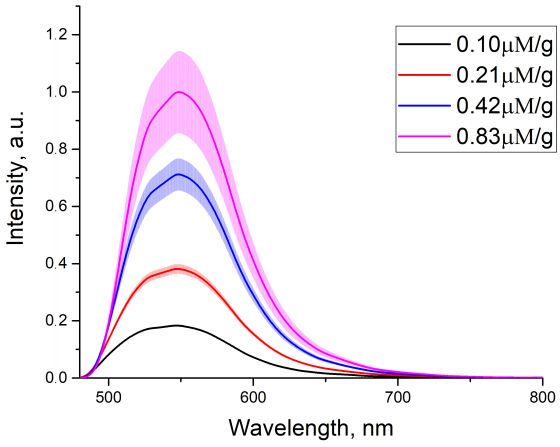
For the three lowest concentrations of riboflavin, it was noticed that the fluorescence intensity recorded by FI decreases proportionally to the decrease of concentrations. However, the same trend was not observed for the highest concentration, which can be caused by reaching such concentration, starting from which the level of fluorescence intensity becomes constant.

The trend calculated from fluorescence images (Fig. 3c) was also confirmed during measurements with FS channel. Future studies will be dedicated to the combining of the fluorescence measurements with hyperspectral technology [52] to develop effective compensation algorithms to attenuate the influence of tissue/phantom light absorbers (e.g. hemoglobin) on the fluorescence intensity recorded.

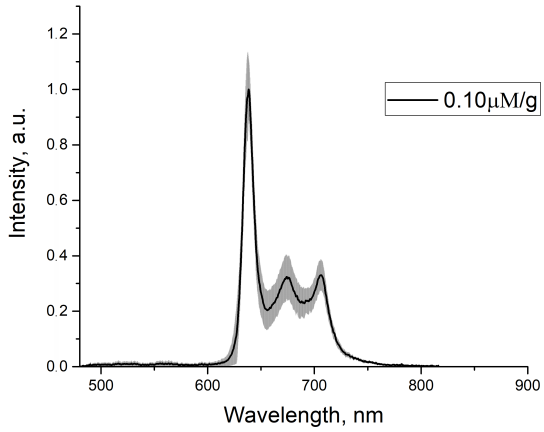
Based on the results presented in Fig. 2 and 3c, a significant effect of uneven illumination of the optical phantom was observed during data processing, which suggests the implementation of orthogonal optical schemes in future research.

3.2 Animal Study

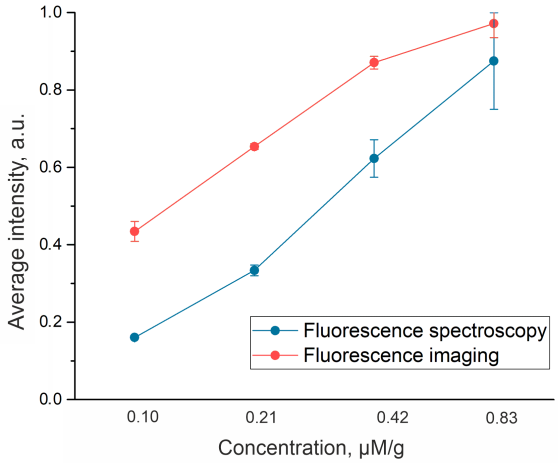
In the course of the study, images of the abdominal cavity of two laboratory animals with an experimental malignant tumor of the liver were obtained.



(a)

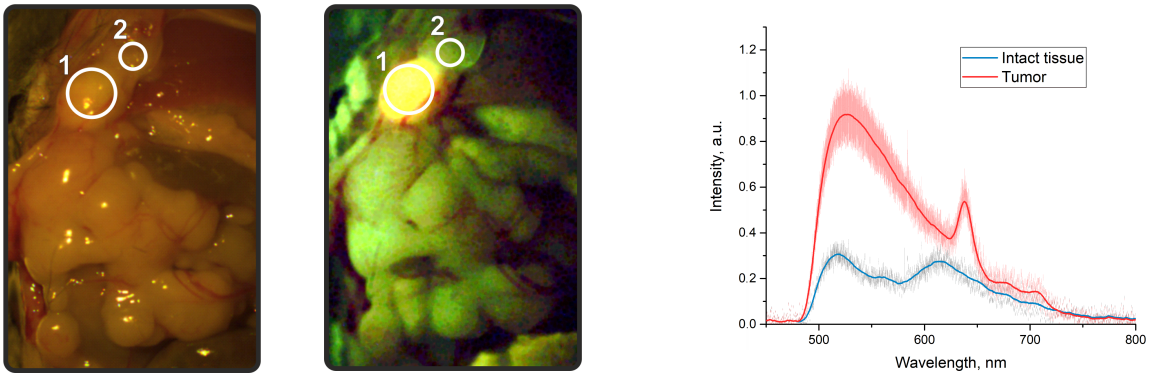


(b)



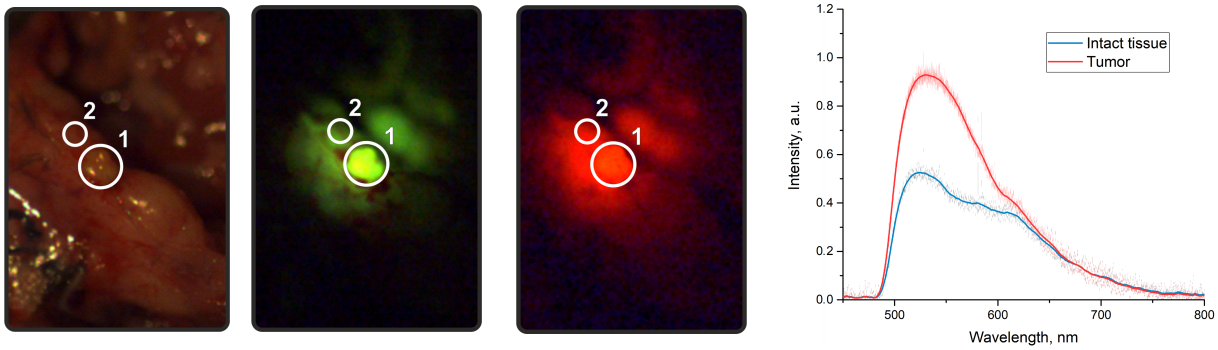
(c)

Fig. 3 Average normalized fluorescence spectra of riboflavin (a) and PpIX (b) solutions, fluorescence intensities curves obtained from FS and FI data (c).



(a) (b) (c)

Fig. 4 The image in white light (a), fluorescence image with 495 nm filter (b) and fluorescence spectra (c) of abdominal cavity of mouse 1.



(a) (b) (c) (d)

Fig. 5 The image in white light (a), fluorescence image with 495 nm filter (b), fluorescence image with 610 nm filter (c) and fluorescence spectra (d) of abdominal cavity of mouse 2.

Fig. 4 and 5 show white images, fluorescence images and fluorescence spectra of target zones. The areas highlighted by a circle 1 correspond to the localization of the tumor. The areas highlighted by a circle 2 correspond to surrounding intact liver tissues. When the light is filtered with 495 nm filter, the fluorescence can be visualized mainly in the range of 500–540 nm. With 610 nm filter, a clear contrast of fluorescence is observed in the range of 620–640 nm.

It should be noted that fluorescence images of mouse 1 were obtained only with 495 nm light filter. The diameter of the probing area was about 3 cm. During the analysis of the initial images of mouse 1, it was noted that the tumor was not green colored as it should be for the peak of FAD fluorescence (about 530 nm). Instead, it was yellow, which was presumably associated with significant accumulation of porphyrins in the tumor and, thus, the summation of fluorescence FAD and porphyrins (fluorescence in the range of 620–640 nm). The FS data confirmed this hypothesis; therefore, FI measurements protocol and experimental setup were upgraded for the second series of measurements. The images of mouse 2 were obtained using two filters.

The values of white light reflectance intensity and fluorescence intensity in the highlighted areas were averaged to compare the data from the tumor and surrounding tissues obtained in white light and fluorescence mode. As a result, it was found that while the intensity of the tumor reflectance exceeded the intensity from unchanged tissue by 1.2 times. Fluorescence images demonstrated the value of this parameter is 4.2 for 495 nm filtered images and 2.6 for 610 nm filtered images. This result proves that it is possible to more clearly distinguish the tumor focus. An increase of fluorescence intensity in malignant tissues compared with the surrounding tissues in 495 nm filtered images may indicate changes in the content of endogenous fluorophores, which in turn are caused by metabolic disorders accompanying carcinogenesis process.

The images of mouse 2 under 495 nm filter did not demonstrate the same pronounced yellow color in the tumor. The fluorescence spectra (Fig. 4c and Fig. 5d) demonstrated that the accumulation of PpIX fluorescence in the tumor of mouse 1 was greater than in mouse 2. Based on the analysis of the obtained images and spectra, it was noticed that the carcinogenesis processes occurred individually in each animal, which should also be taken into account when planning and conducting further experimental studies.

Thus, the obtained images and the calculated differences in the tumor/intact tissue ratio of average fluorescence intensity indicate a high sensitivity of FI technique to the presence of malignant changes in the tissues compared to conventional images recorded in white light. Depending on the fluorescence intensity increase degree, a more accurate determination of the accumulation sites of various fluorophores in the tissue structure of the organ is possible *in vivo*. At the same time, the FS method can also provide additional information for the correct interpretation of the FI data. In this regard, the use of hyperspectral technologies for measuring the fluorescence of biological tissues is promising.

4 Conclusion

Many researchers work on the development of technical implementation and diagnostic criteria for intraoperative fluorescence imaging based on the autofluorescence of endogenous fluorophores. An important stage of such research is the providing of reproducible measurements of biological tissues for both the process of development itself and for primary and periodic calibration of imaging systems during their practical application.

For these purposes, we developed the experimental setup for fluorescence imaging of tissues fluorophores associated with metabolic changes and carcinogenesis. The optical phantom mimicking the biological tissue fluorescence was also created for its calibration as a preliminary stage of complex development of FI technology for cancer detection during surgery.

These studies showed the possibility of application of the developed fluorescence imaging system for obtaining real-time information about the presence of malignant cells on the resection margin in cancer surgery. The implementation of FI technology to clinical practice can increase the effectiveness of surgical interventions in the long term by reducing time spend on surgeries and reducing the probability of a false negative error during the defining of the resection margin.

The proposed phantom is relatively simple to manufacture and use for measurements. The phantom mimics tissue fluorescence for specific research tasks, taking into account the presence of collagen. As an option for further research in this direction, it is planned to develop a more complex optical model of biological tissue using other endogenous fluorophores, such as NADH and FAD themselves. The obtained experimental data indicate the sensitivity of the developed fluorescence phantom to changes in the concentration of flavins, as well as the presence of PpIX.

Application of the developed optical phantom will allow to more accurately test the FI systems and improve the overall quality of implementation of this technology. The data obtained will be used to correct fluorescence images of pathological biological tissues and to more clearly determine the resection margins. Further research will be aimed at improving the technical implementation and the optical phantom, as well as conducting reliable and reproducible experimental measurements of normal and tumor tissue parameters to develop diagnostic criteria and introduce fluorescence imaging technology into clinical practice.

Disclosures

All authors declare that there is no conflict of interests in this paper.

Acknowledgments

The study was supported by the Russian Foundation for Basic Research according to the research project 18-02-00669. VD acknowledges for personal support from the European Union's Horizon 2020 research and innovation program under the Marie Sklodowska-Curie grant agreement No. 839888. Authors are very grateful to Dr. Olga V. Morozova (N. N. Blokhin National Medical Research Center of Oncology, Moscow, Russia) for tumor cell inoculation.

References

1. R. F. Bray, J. Ferlay, I. Soerjomataram, R. L. Siegel, L. A. Torre, and A. Jemal, "Global cancer statistics 2018: GLOBOCAN estimates of incidence and mortality worldwide for 36 cancers in 185 countries," CA: A Cancer Journal for Clinicians 68(6), 394–424 (2018).
2. S. Lin, K. Hoffmann, and P. Schemmer, "Treatment of hepatocellular carcinoma: a systematic review," Liver cancer 1(3–4), 144–158 (2012).
3. N. Coburn, R. Cosby, L. Klein, G. Knight, R. Malthaner, J. Mamazza, C. D. Mercer, and J. Ringash, "Staging and surgical approaches in gastric cancer: A systematic review," Cancer Treatment Reviews 63, 104–115 (2018).
4. K. D. Miller, L. Nogueira, A. B. Mariotto, J. H. Rowland, K. R. Yabroff, C. M. Alfano, A. Jemal, J. L. Kramer, and R. L. Siegel, "Cancer treatment and survivorship statistics, 2019," CA: A Cancer Journal for Clinicians 69(5), 363–385 (2019).
5. K. J. Chambers, S. Kraft, and K. Emerick, "Evaluation of frozen section margins in high-risk cutaneous squamous cell carcinomas of the head and neck," Laryngoscope 125(3), 636–639 (2015).
6. E. L. Rosenthal, J. M. Warram, E. de Boer, J. P. Basilion, M. A. Biel, M. Bogyo, M. Bouvet, B. E. Brigman, Y. L. Colson, S. R. DeMeester, G. C. Gurtner, T. Ishizawa, P. M. Jacobs, S. Keereweer, J. C. Liao, Q. T. Nguyen, J. M.

Olson, K. D. Paulsen, D. Rieves, B. D. Sumer, M. F. Tweedle, A. L. Vahrmeijer, J. P. Weichert, B. C. Wilson, M. R. Zenn, K. R. Zinn, and G. M. van Dam, "Successful translation of fluorescence navigation during oncologic surgery: a consensus report," Journal of Nuclear Medicine 57(1), 144–150 (2016).
7. I. J. Bigio, J. R. Mourant, "Optical biopsy," in Encyclopedia of Optical Engineering, CRC Press, Boca Raton, 1577–1593 (2003).
8. T. D. Wang, J. Van Dam, "Optical biopsy: A new frontier in endoscopic detection and diagnosis," Clinical Gastroenterology and Hepatology 2(9), 744–753 (2004).
9. G. T. Kennedy, O. T. Okusanya, J. J. Keating, D. F. Heitjan, C. Deshpande, L. A. Litzky, S. M. Albelda, J. A. Drebin, S. Nie, P. S. Low, and S. Singhal, "The optical biopsy: A novel technique for rapid intraoperative diagnosis of primary pulmonary adenocarcinomas," Annals of Surgery 262(4), 602–609 (2015).
10. A. C. Croce, A. Ferrigno, G. Bottiroli, and M. Vairetti, "Autofluorescence-based optical biopsy: An effective diagnostic tool in hepatology," Liver International 38(7), 1160–1174 (2018).
11. I. Georgakoudi, M. S. Feld, "The combined use of fluorescence, reflectance, and light-scattering spectroscopy for evaluating dysplasia in Barrett's esophagus," Gastrointestinal Endoscopy Clinics of North America 14(3), 519–537 (2004).
12. S. Y. Lee, W. R. Lloyd, M. Chandra, R. H. Wilson, B. McKenna, D. Simeone, J. Scheiman, and M.-A. Mycek, "Characterizing human pancreatic cancer precursor using quantitative tissue optical spectroscopy," Biomedical Optics Express 4(12), 2828–2834 (2013).
13. A. Gisbrecht, E. Borisova, T. Genova-Hristova, P. Troyanpva, E. Pavlova, N. Penkov, I. Bratchenko, V. Zakharov, I. Lihachova, I. Kuzmina, and J. Spigulis, "Multispectral autoflourescence detection of skin neoplasia using steady-state techniques," Proceeding of SPIE 11047, 1104704 (2019).
14. Y. A. Khristoforova, I. A. Bratchenko, O. O. Myakinin, D. N. Artemyev, A. A. Moryatov, A. E. Orlov, S. V. Kozlov, and V. P. Zakharov, "Portable spectroscopic system for in vivo skin neoplasms diagnostics by Raman and autofluorescence analysis," Journal of Biophotonics 12(4), e201800400 (2019).
15. K. Kandurova, V. Dremin, E. Zherebtsov, E. Potapova, A. Alyanov, A. Mamoshin, Y. Ivanov, A. Borsukov, and A. Dunaev, "Fiber-optic system for intraoperative study of abdominal organs during minimally invasive surgical interventions," Applied Sciences 9(2), 217 (2019).
16. V. R. Kolli, A. R. Shaha, H. E. Savage, P. G. Sacks, M. A. Casale, and S. P. Schantz, "Native cellular fluorescence can identify changes in epithelial thickness in-vivo in the upper aerodigestive tract," The American Journal of Surgery 170(5), 495–498 (1995).
17. B. Hill, S. F. Lam, P. Lane, C. MacAulay, L. Fradkin, and M. Follen, "Established and emerging optical technologies for the real-time detection of cervical neoplasia: a review," Journal of Cancer Therapy 8(13), 1241–1278 (2017).
18. K. He, L. Zhao, Y. Chen, X. Huang, Y. Ding, H. Hua, L. Liu, X. Wang, M. Wang, Y. Zhang, and Z. Fan, "Label‐free multiphoton microscopic imaging as a novel real‐time approach for discriminating colorectal lesions: A preliminary study," Journal of Gastroenterology and Hepatology 34(12), 2144–2151 (2019).
19. T. Nagaya, Y. A. Nakamura, P. L. Choyke, and H. Kobayashi, "Fluorescence-guided surgery," Frontiers in Oncology 7, 314 (2017).
20. K. Koenig, H. Schneckenburger, "Laser-induced autofluorescence for medical diagnosis," Journal of Fluorescence 4(1), 17–40 (1994).
21. S. Palmer, K. Litvinova, A. Dunaev, J. Yubo, D. McGloin, and G. Nabi, "Optical redox ratio and endogenous porphyrins in the detection of urinary bladder cancer: A patient biopsy analysis," Journal of Biophotonics 10(8), 1062–1073 (2017).
22. T. Vo-Dinh, Biomedical photonics handbook: biomedical diagnostics, CRC press, Boca Raton (2014).
23. K. T. Moesta, B. Ebert, T. Handke, D. Nolte, C. Nowak, W. E. Haensch, R. K. Pandey, T. J. Dougherty, H. Rinneberg, and P. M. Schlag, "Protoporphyrin IX occurs naturally in colorectal cancers and their metastases," Cancer Research 61(3), 991–999 (2001).
24. C. J. Fox, P. S. Hammerman, and C. B. Thompson, "Fuel feeds function: energy metabolism and the T-cell response," Nature Reviews Immunology 5(11), 844–852 (2005).
25. E. Currie, A. Schulze, R. Zechner, T. C. Walther, and R. V. Farese, "Cellular fatty acid metabolism and cancer," Cell Metabolism 18(2), 153–161 (2013).
26. Y. Wu , P. Xi, J. Y. Qu, T.-H. Cheung, and M.-Y. Yu, "Depth-resolved fluorescence spectroscopy of normal and dysplastic cervical tissue," Optics Express 13(2), 382–388 (2005).
27. Y. Wu, J. Y. Qu, "Autofluorescence spectroscopy of epithelial tissues," Journal of Biomedical Optics 11(5), 054023 (2006).
28. N. Ramanujam, "Fluorescence spectroscopy of neoplastic and non-neoplastic tissues," Neoplasia 2(1–2), 89–117 (2000).
29. M. M. Lukina, M. V. Shirmanova, T. F. Sergeeva, and E. V. Zagaynova, "Metabolic imaging in the study of oncological processes," Sovremennye Tehnologii v Medicine 8(4 (eng)), 113–124 (2016).

30. I. Pavlova, K. Sokolov, R. Drezek, A. Malpica, M. Follen, and R. Richards-Kortum, "Microanatomical and Biochemical Origins of Normal and Precancerous Cervical Autofluorescence Using Laser - scanning Fluorescence Confocal Microscopy," Photochemistry and Photobiology 77(5), 550–555 (2003).
31. A. C. Croce, G. Santamaria, U. D. Simone, F. Lucchini, I. Freitas, and G. Bottiroli, "Naturally-occurring porphyrins in a spontaneous-tumour bearing mouse model," Photochemical & Photobiological Sciences 10(7), 1189–1195 (2011)..
32. W. Kemmner, K. Wan, S. Rüttinger, B. Ebert, R. Macdonald, U. Klamm, and K. T. Moesta, "Silencing of human ferrochelatase causes abundant protoporphyrin-IX accumulation in colon cancer," The FASEB Journal 22(2), 500–509 (2008).
33. M. Sachar, K. E. Anderson, and X. Ma, "Protoporphyrin IX: the good, the bad, and the ugly," Journal of Pharmacology and Experimental Therapeutics 356(2), 267–275 (2016).
34. E. A. Machinskaya, V. I. Ivanova-Radkevich, "Review of selective accumudation of photosensitizers with different chemical structure in tumor tissue," Photodynamic therapy and photodyagnosis 2(4), 28–32 (2013). [in Russian]
35. A. Moiyadi, P, Shetty, E. Sridhar, V. Gota, M. Gurjar, G. Saicharan, V. Singh, and S. Srivastava, "Objective assessment of intraoperative tumor fluorescence reveals biological heterogeneity within glioblastomas: a biometric study," Journal of Neuro-Oncology 146(3), 477–488 (2020).
36. O. Stelmashchuk, E. Zherebtsov, A. Zherebtsova, E. Kuznetsova, A. Vinokurov, A. Dunaev, A. Mamoshin, I. Snimshchikova, A. Borsukov, A. Bykov, and I. Meglinski, "Noninvasive control of the transport function of fluorescent coloured liposomal nanoparticles," Laser Physics Letters 14(6), 065603 (2017).
37. I. V. Meglinski, S. J. Matcher, "Quantitative assessment of skin layers absorption and skin reflectance spectra simulation in the visible and near-infrared spectral regions," Physiological Measurement 23(4), 741 (2002).
38. P. Thueler, I. Charvet, F. Bevilacqua, M. St. Ghislain, G. Ory, P. Marquet, P. Meda, B. Vermeulen, and C. Depeursinge, "In vivo endoscopic tissue diagnostics based on spectroscopic absorption, scattering, and phase function properties," Journal of Biomedical Optics 8(3), 495–504 (2003).
39. M. Anastasopoulou, D. Gorpas, M. Koch, E. Liapis, S. Glasl, U. Klemm, A. Karlas, T. Lasser, and V. Ntziachristos, "Fluorescence imaging reversion using spatially variant deconvolution," Scientific Reports 9(1), 1–11 (2019).
40. L. H. Luthjens, T. Yao, and J. M. Warman, "A polymer-gel eye-phantom for 3D fluorescent imaging of millimetre radiation beams," Polymers 10(11), 1195 (2018).
41. H. Lu, F. Floris, M. Rensing, and S. Andersson-Engels, "Fluorescence spectroscopy study of protoporphyrin IX in tissue-like phantoms," Proceeding of SPIE 11190, 111901S (2019).
42. Y. Xie, E. Maneas, S. Islam, W. Peveler, J. Shapey, W. Xia, S. Ourselin, I. P. Parkin, A. E. Desjardins, and T. Vercauteren, "Soft optically tuneable fluorescence phantoms based on gel wax and quantum dots: a tissue surrogate for fluorescence imaging validation," Proceeding of SPIE 10862, 108621F (2019).
43. U. Resch-Genger, M. Grabolle, S. Cavaliere-Jaricot, R. Nitschke, and T. Nann, "Quantum dots versus organic dyes as fluorescent labels," Nature Methods 5(9), 763–775 (2008).
44. M. Anastasopoulou, M. Koch, V. Ntziachristos, D. Gorpas, P. B. Garcia-Allende, U. Klemm, and A. Karlas, "Multiparameter solid phantom for fluorescence imaging standardization," Proceeding of SPIE 10411, 104110J (2017).
45. B. W. Pogue, M. S. Patterson, "Review of tissue simulating phantoms for optical spectroscopy, imaging and dosimetry," Journal of Biomedical Optics 11(4), 041102 (2006).
46. B. Leh, R. Siebert, H. Hamzeh, L. Menard, M.-A. Duval, Y. Charon, and D. A. Haidar, "Optical phantoms with variable properties and geometries for diffuse and fluorescence optical spectroscopy," Journal of Biomedical Optics 17(10), 108001 (2012).
47. K. B. Nivetha, N. Sujatha, "Development of thin skin mimicking bilayer solid tissue phantoms for optical spectroscopic studies," Biomedical Optics Express 8(7), 3198–3212 (2017).
48. P. Drössler, W. Holzer, A. Penzkofer, and P. Hegemann, "pH dependence of the absorption and emission behaviour of riboflavin in aqueous solution," Chemical Physics 282(3), 429–439 (2002).
49. A. Aliverti, B. Curti, and M. A. Vanoni, "Identifying and quantitating FAD and FMN in simple and in iron-sulfur-containing flavoproteins," in Flavoprotein Protocols, S. K. Chapman, G. A. Reid (eds.), Springer, New York, 9–23 (1999).
50. M. L. Dean, T. A. Miller, and C. Brückner, "Egg-citing! Isolation of protoporphyrin IX from brown eggshells and its detection by optical spectroscopy and chemiluminescence," Journal of Chemical Education 88(6), 788–792 (2011).
51. OECD Series on Principles of Good Laboratory Practice (GLP) and Compliance Monitoring, Organisation for Economic Co-operation and Development, Paris, France, 1998–2019 (accessed 14.02.2020).
52. E. Zherebtsov, V. Dremin, A. Popov, A. Doronin, D. Kurakina, M. Kirillin, I. Meglinski, and A. Bykov, "Hyperspectral imaging of human skin aided by artificial neural networks," Biomedical Optics Express 10(7), 3545–3559 (2019).

Practical implementation analysis of the fractal dimension calculating algorithm for the medical images by the example of neutrophil nuclei

Semen A. Naydenov[1*], Pavel A. Naydenov[2], and Elena V. Shevchenko[1]
[1] Irkutsk State Medical University, 1 Krasnogo Vosstaniya st., Irkutsk 664003, Russia
[2] Irkutsk State University, 1 Karl Marx st., Irkutsk 664003, Russia

*** e-mail:** semen.naid@yandex.ru

Abstract. This paper presents the results of estimating the fractal dimension of neutrophil nuclei to determine their functional state. Calculations were carried out by a specially developed software-implemented algorithm. The study has shown that the fractal theory can be applied to automate medical image processing. © 2020 Journal of Biomedical Photonics & Engineering.

Keywords: fractals; image processing; neutrophils; medical images.

Paper #3346 received 15 Jan 2020; revised manuscript received 15 Mar 2020; accepted for publication 17 Mar 2020; published online 24 Mar 2020. doi: 10.18287/JBPE20.06.010304.

1 Introduction

Nowadays, investigations into medical images have become well established in clinical diagnostics of various pathologies. Thus, the use of X-ray radiation, acoustic waves, laser radiation, microscopic and computer-assisted studies for obtaining images, has considerably expanded the possibilities of contemporary healthcare [1, 2]. Development and implementation of a detailed mathematical image processing methodology, be it microphotography or an X-ray picture, by utilizing electronic computer systems, will considerably increase processing efficiency [3]. One of the numerical methods to process nonlinear images, including medical images, is estimating their fractal dimension [4, 5]. This method is actively used both in Russia and internationally [6–10]. However, to our knowledge, there has not been any research on utilizing fractal analysis for neutrophil images, which can testify the relevance of this study.

Current clinical practice makes wide use of White Blood Cell Differential Count – percentage ratio of various leukocyte types, especially different neutrophil forms, when they are counted in a stained blood smear under a microscope.

Neutrophil granulocytes (neutrophil leukocytes, neutrophils) is the most numerous group of leukocytes. The reference values of their blood level are within 2.0 to 5.5 × 10^9 per 1 L (which makes up from 48 to 78% of the total leukocyte number). The nucleus of a mature segmented neutrophil contains 3–5 segments connected by thin filaments. In blood, there are neutrophils of three types of maturity: metamyelocytes (juvenile neutrophils), band neutrophils and segmented neutrophils. Metamyelocytes and band neutrophils qualify as young cells. Under normal conditions, the metamyelocyte level does not exceed 0.5% and is characterized with a kidney bean shaped nucleus. Band neutrophils under normal conditions make up from 1 to 6% of the total number of leukocytes, have an unsegmented nucleus often of a horseshoe shape or *S*-shape. Increased percentage of metamyelocytes and band neutrophils may indicate the presence of an acute pyoinflammatory process or acute vast blood loss. This is caused by accelerated hemopoiesis process and by replacement of the lost cells with younger forms [11].

Hence, the neutrophil classification and percentage calculation for each type present an important clinical test. Moreover, the cell type and age are directly connected with the nucleus structure, particularly with its segmentation, which in today's clinical practice is determined by physicians visually and subjectively. In addition, microscopic analysis of blood smears in conditions of an ordinary hospital is now quite laborious due to a large number of patients.

Therefore, the aim of this study is to develop an automated method for medical image processing based on fractal analysis, which could cover the microscopic analysis of blood smears as well.

2 Materials and Methods

The materials for this study were fixed and routine stained blood smears in patients of the Surgery Department of Irkutsk Research Center of Surgery and Traumatology (Russia). Blood was collected before and after surgery. The blood smears were stained by

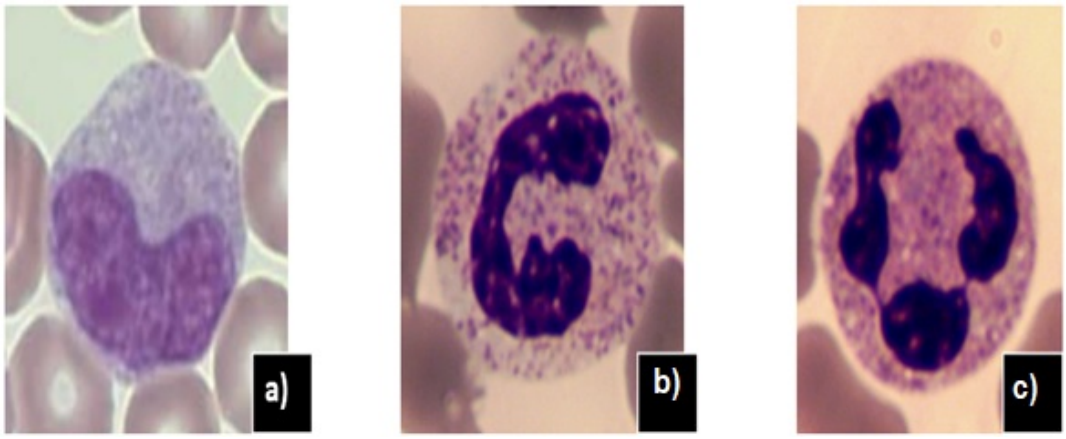


Fig. 1 Neutrophils in the blood smear: a) Metamyelocyte, b) Band neutrophil, c) Segmented neutrophil.

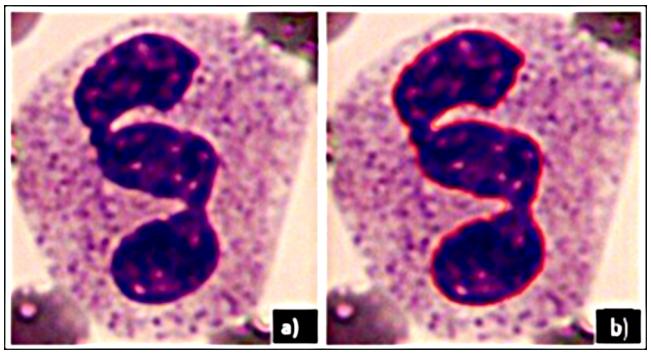


Fig. 2Iimage pre-processing: a) before processing, b) after processing.

Romanowsky–Giemsa solution for 20 minutes. The protocols of the investigation were approved by the medicine ethical committee of Irkutsk State Medical University.

The prepared smears were viewed and microphotographed by the Altami-163t microscope equipped with the Levenhuk C-Series digital camera with the resolution of 2048 × 1546 px. The cells were viewed at 2000× magnification.

The fractal dimension was calculated by a specially developed programmable algorithm.

For the purpose of sampling, the cells were classified into metamyelocytes, band granulocytes and segmented granulocytes. The neutrophils were classified according to the morphological characteristics of the granulocytic lineage cells presented below [12].

Metamyelocytes (Fig. 1a) has the cell size of 10 to 16 μm. The nucleus is of kidney-bean shape and lilac color. The cytoplasm is pale pink, smoke-grey or light blue. Inside, the cell has neutrophil granularity evenly spread over the cytoplasm.

Band neutrophils (Fig. 1b) has the cell size is 9 to 12 μm. The nucleus is of curved band shape and of purple color. The chromatin has a crude structure. The cytoplasm is pink with a purple shade. Inside, it is characterized by neutrophil granularity, often unevenly spread over the cytoplasm.

Segmented neutrophils (Fig. 1c) has the cell size is 9 to 12 μm. The nucleus is of irregular shape, polymorphic, segmented (with 2 to 5 lobes) and bright purple. Between the lobes there are thin connecting filaments. The cell cytoplasm is pink or pink purple with neutrophil granularity.

The fractal dimension calculation based on the covering method [4, 5] was performed by specially developed algorithm that is described, step-by-step, below.

1. The image is pre-processed by means of a graphic editor as shown in Fig. 2.

2. The fractal dimension is calculated by specially developed software (Fig. 3) written and implemented using Borland Delphi 7 platform.

Below is the general equation for calculating fractal dimension [4]:

$$D = -\lim_{\varepsilon \to 0} \frac{\log\big(N(\varepsilon)\big)}{\log\left(\frac{1}{\varepsilon}\right)},$$

where D is fractal dimension, N is the number of boxes Ɛ, Ɛ is the box size.

Image pre-processing was performed by the means of Adobe Photoshop CS 6, Stroke tool, 2 px stroke width, red color (R-255, G-0, B-0; #ff0000). The Ɛ box size was set in px (5 px and more).

The program includes a set of commands that perform the following tasks:

1. Uploading the image to be processed from a prepared file.

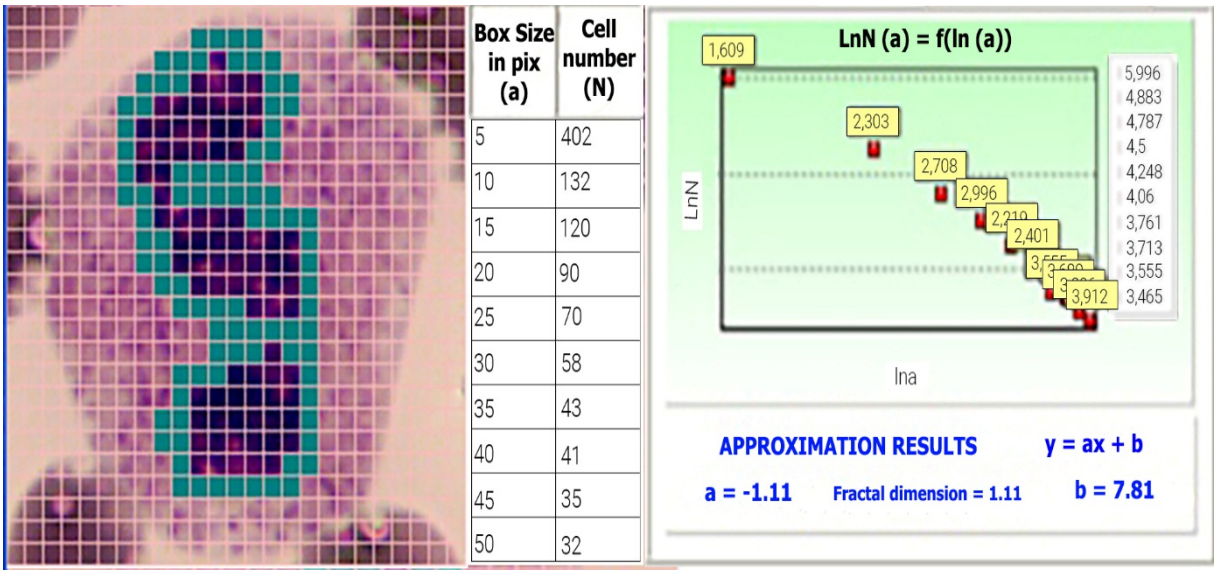


Fig. 3 Calculation of fractal dimension by means of specially developed software.

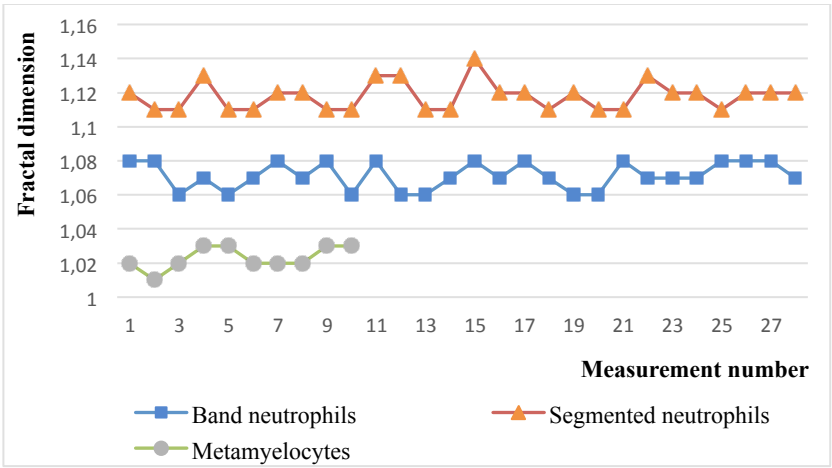


Fig. 4 Comparison of the values of fractal dimension for neutrophil nuclei.

2. Building matrices above the uploaded image. The matrices consist of square boxes of a certain size measured in pixels.

3. Along with building the matrices, the program is counting the boxes whose area contains at least one pixel of the outline under examination.

4. Building a graph based on the calculated data with simultaneous calculating the fractal dimension.

3 Results

The results of calculating the neutrophil fractal dimension are presented in Fig. 4. The x-axis represents the measurement number where each measurement corresponds to a new sample. Consequently, the following types of neutrophils were examined: 28 band neutrophils, 28 segmented neutrophils and 10 metamyelocytes.

The graph shows no crossing of fractal dimension values for neutrophils belonging to three various groups according to their morphological characteristics: for band neutrophils, the nucleus fractal dimension is ranging between 1.06 and 1.08. For segmented neutrophils, the nucleus fractal dimension is ranging between 1.11 and 1.14. For metamyelocytes, the nucleus fractal dimension is ranging between 1.01 and 1.03. The confidence interval was estimated using a standard method for small samples.

The obtained data were processed through estimating Student's coefficient for independent variables. Comparison of the critical and empirical t-tests has demonstrated statistical significance of differences between the nucleus fractal dimension of metamyelocytes, segmented neutrophils and band neutrophils.

This result reflects the fact that fractal dimension is not dependent on the nucleus size of the samples but on their shape. The fractal method is able to estimate the extent of the object 'unevenness, i.e., in fact, to numerically determine and distinguish what a physician determines intuitively examining the sample with a microscope. The suggested algorithm for estimating the nuclear fractal dimension is able to automatically determine the neutrophil types and, consequently, to

divide the neutrophils into band neutrophils, segmented neutrophils and metamyelocytes.

4 Conclusion

The study has shown the possibility to apply the fractal theory for automating medical image processing. A new algorithm has been developed for computer-assisted calculation of the fractal dimension for medical images. The fractal dimension of the neutrophil nuclei is dependent on their age:

- for metamyelocytes, the values of the fractal dimension are ranging between 1.01 and 1.03;
- for band neutrophils, they are ranging between 1.06 and 1.09;
- for segmented neutrophils, they are ranging between 1.11 and 1.14.

Fractal dimension has proved to be a sufficient parameter for determining the neutrophil type and is independent of the patient's individual characteristics.

Disclosures

All authors declare that there is no conflict of interests in this paper.

References

1. V. V. Goryunova. T. I. Goryunova. I. I. Kukhtevich, and T. T. Polyakova, "Processing medical images in graph databases and patient identification," Mezhdunarodnyy studencheskiy nauchnyy vestnik 4(9), 1390–1393 (2017) [in Russian].
2. S. V. Ablameyko, A. M. Nedzved, Processing optical images of cell structures in medicine, OIPI NAN Belarusi, Minsk (2005) [in Russian].
3. N. N. Chernov, A. P. Samoylenko, and A. V. Pribylskiy, "A technique to increase the informative value of X-ray image pre-processing," Modelirovaniye, optimizatsiya i informatsionnyye tekhnologii 6(1), 6–20 (2018) [in Russian]..
4. A. K. Ostapchuk, V. E. Ovsyannikov, Application of fractal theory in mathematical modelling and equipment, Izdetelstvo Kurganskogo gosudarstvennogo universiteta, Kurgan (2009) [in Russian].
5. P. Nesterov, "Calculating Minkowskian fractal dimension for 2D-imaging," Habr (accessed 15.12.2018) [in Russian].
6. A. I. Povoroznyuk, A. V. Emelianova, "A system of medical image processing in radiology by means of fractal analysis," Vestnik NTU "KhPI" 35, 147–151 (2014) [in Russian].
7. G. S. Simonyan, A. G. Simonyan, "Fractality of biological systems. II Fractality of cells and cell ensembles," Mezhdunarodnyy zhurnal prikladnykh i fundamentalnykh issledovaniy 3(2), 268–271 (2016) [in Russian].
8. P. Bose, N. T. Brockton, K. Guggisberg, S. C. Nakoneshny, E. Kornaga, A. C. Klimowicz, M. Tambasco, and J. C. Dort, "Fractal analysis of nuclear histology integrates tumor and stromal features into a single prognostic factor of the oral cancer microenviroment," BMC Cancer 15(1), 409–418 (2015).
9. S. Bhandari, S. Choudannavar, E. R. Avery, P. Sahay, and P. Pradhan "Detection of colon cancer stages via fractal dimension analysis of optical transmission imaging of tissue microarrays (TMA)," Biomedical Physics & Engineering Express 4(6), 65–75 (2018).
10. K. Metze, R. Adam, J. B. Florindo, "The fractal dimension of chromatin - a potential molecular marker for carcinogenesis, tumor progression and prognosis," Expert Review of Molecular Diagnostics 19(4), 299–312 (2019).
11. Yu. I. Afanasyev, N. A. Yurina, and E. F. Kotovskiy, Histology, cytology and embryology, Meditsina, Moscow (2002) [in Russian].
12. Laboratory diagnostics (accessed 29.11.2018).
13. P. S. Aleksandrov, P. S. Uryson, Memoir on compact topological spaces, Fizmatlit, Moscow (2009) [in Russian].
14. B. Mandelbrot, Fractal geometry of nature, Institut Kompyuternykh Issledovaniy, Moscow (2002) [in Russian].

Solid-phase luminescence of pyrene in chitosan adsorbents

Danila A. Tatarinov*, Sofia R. Sokolnikova, and Natalia A. Myslitskaya
Department of Physics, Kaliningrad State Technical University, 1 Sovetsky prospect, Kaliningrad 236022, Russia

*** e-mail:** dan.tatarinov@mail.ru

Abstract. The preparation method of modified chitosan films for adsorption of pyrene from solution is described. Solid-phase luminescence of samples was studied, degree of extraction and index of polarity of microenvironment of pyrene molecules was determined. It has been proven possible to carry out luminescent analysis of substances for pyrene content using made films. The observed results demonstrate an ability for the using method of solid-phase luminescence (SPL) to increase the range of optical transparency and avoid pre-extraction and concentration of the test samples. © 2020 Journal of Biomedical Photonics & Engineering.

Keywords: Luminescent analysis; pyrene; polycyclic aromatic hydrocarbons; surfactants; solid-phase luminescence; chitosan.

Paper #3342 received 12 Jan 2020; revised manuscript received 19 Mar 2020; accepted for publication 19 Mar 2020; published online 25 Mar 2020. doi: 10.18287/JBPE20.06.010305.

1 Introduction

Nowadays, polycyclic aromatic hydrocarbons (PAH) are one of the most dangerous carcinogens. The reason for PAH formation is pyrolysis of organic substances. The mechanism of toxicity is considered to be interference with the function of cellular membranes as well as with enzyme systems that are associated with the membrane. It has been proved that PAH can cause carcinogenic and mutagenic effects and are potent immunosuppressants. Effects have been documented on immune system development, humoral immunity and on host resistance. PAH are accumulated in the human body and cause a change in the structure of DNA, which results in cancer. [1]. In this regard, the selected topic is relevant in modern environmental conditions for the protection of human health [2–4].

Due to their bioaccumulation capacity, substances of the PAH group are potentially dangerous for humans even at low concentrations. According to Russian standards for monitoring PAH content, the level of content of one of the most common representatives of these substances is measured – benz(a)pyrene (BP) [5]. Maximum permissible average daily concentrations of BP in atmospheric air is 0.001 mg/l, in soil is 0.02 mg/kg, for majority of food is not more than 1 μg/kg [6].

In laboratory conditions the representative of PAH – pyrene was the most widely used for the study of PAH content in environmental objects. It has features of the electron-vibrational structure of its radiation spectrum, which is characterized by five well resolved main vibrational bands [2]. Also, pyrene has similar fluorescence spectra to one of the most dangerous PAH – BP but is not so toxic that it facilitates its use in laboratory studies [3].

Determination of PAH content is a complex analytical task due to low concentrations of these substances in the environment, and modern methods of analysis are used to solve it [7]. High-performance liquid chromatography is most commonly used for PAH detection. Significant disadvantages of this method are the high cost and the time required to analyze samples. Recent scientific developments make it possible to create more sensitive, reliable and express methods of PAH control. One developing method of PAH detection is luminescent analysis [8].

It has been previously found [7, 9] that in order to increase luminescence intensity, it is effective to use a micellar concentration of pyrene in aqueous solution, but this method allows us to study only liquid substances having sufficient optical transparency. Therefore, SPL was chosen to study substances with large optical transparency ranges.

The SPL method is widely used to determine many inorganic and organic compounds [10–11]. SPL allows us to combine sorption concentration of substances (solid-phase extraction) with their next luminescent determination directly in the sorbent phase that increases sensitivity of the method. Thus, it is possible to research samples in different aggregate states and having different optical transparency [2].

The aim of the study is to research the luminescent properties of pyrene in a fluorescent assay method using

solid chitosan matrices and to study the question of their further modification.

2 Materials and methods

Various materials are used as bases for solid matrices, such as cellulose [12], cellulose acetates [13], chitosan [14]. One of the most promising bases is chitosan, it is a polysaccharide produced by partial deacetylation of chitin, which is a structural element of the exoskeleton of insects, crustaceans and cell walls of fungi [15]. Chitosan is producing in large quantities, thus it has a low cost. It is known chitosan matrices exhibit high sorption capacity [16] and are effective sorbents of heavy metal ions, surfactants, PAHs, etc. [14].

In this study chitosan (Diaham LLC, 95% deacetylation degree) was used as a base for a solid matrix. Chitosan solution at a concentration of 25 g/l was prepared in a 2% acetic acid solution. The solution were poured into each Petri dish and allowed to dry at room temperature for 72 h (Fig. 1a). Also, a few samples were modified with polyvinyl alcohol (PVA) and the surfactant cetyltrimethylammonium bromide (CTAB).

After drying chitosan-based films were kept in 5% aqueous KOH solution to convert the biopolymer to the basic (hydrophobic) form (Fig. 1b). The samples were washed in distilled water with pH = 7 and dried at a temperature of t = 20 °C and a relative humidity of 60% for further studies.

Dimensions of films after drying are d = 5 cm, thickness h = 0.1 ÷ 0.3 mm. After the films are made hydrophobic, the linear dimensions increase slightly. For luminescent analysis 1 × 1 cm samples were prepared from the films and fixed to the slide.

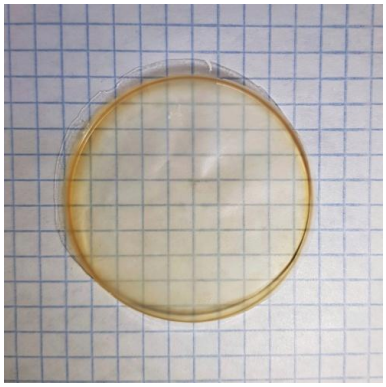
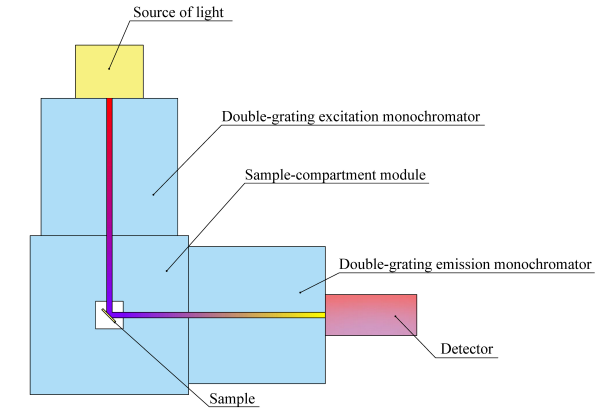


Fig. 1 Chitosan film in hydrophobic form.

A modular system HORIBA Fluorolog-3 TCSPC was used for luminescent analysis. The modular system is shown in Fig. 2. Error of measured parameters consists of error of emission monochromator and error of luminescence intensity measurement. The HORIBA manufacturer stated error value of monochromator emission ±0.5 nm [17].

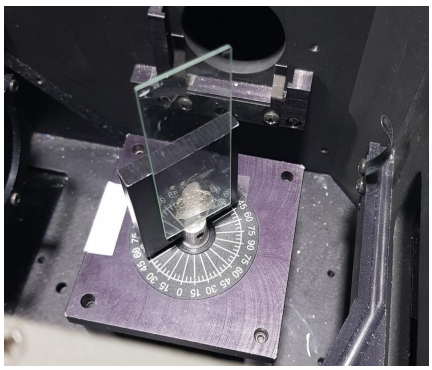
Statistical processing of experimental results was performed using the method IUPAC [18]. For a sample population with degrees of freedom n = 5, root mean square deviation was calculated. Then confidence interval about the mean with confidence level 0.95 and error of result were determined. For the polarity index the absolute error was 0.03–0.05, and for the extent of pyrene extraction the absolute error was 2–4 %.



a



b



c

Fig. 2 (a) scheme of HORIBA Fluorolog-3 TCSPC; (b) modular system HORIBA Fluorolog-3 TCSPC; (c) sample of film in modular system HORIBA.

Spectral characteristics of PAH in aqueous solution and sorbed onto the solid surface were studied on the example of pyrene having similar luminescence spectra with BP. Pyrene was dissolved in a dimethyl sulfoxide (DMSO) solution at a concentration of 10^{-6} mol/l. Test sample solutions were prepared on distilled water

pH = 7. The obtained films were kept in the prepared solution, then the samples were dried.

3 Results and discussion

The results of fluorescent analysis of films after static sorption in DMSO and pyrene solution are shown in Fig. 3. The resulting spectra are represented by five vibron bands in the wavelength range of 372 nm to 393 nm, which represent the characteristic fluorescence spectrum of pyrene [19].

Films of pure chitosan are very brittle and not very convenient to use. Various additives are used to improve their mechanical properties [20].

In this work, modified matrices were developed using CTAB (C = 0.01 M), and a solution of PVA (synthetic water-soluble polymer, C = 5%) was added to increase strength. Graphs show chitosan films are capable of effectively adsorbing pyrene, also the fluorescence intensity of modified films is significantly higher than that of unmodified chitosan film without additives.

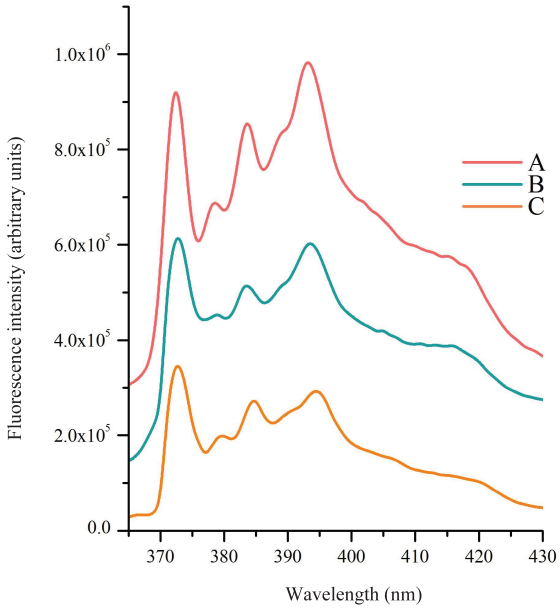


Fig. 3 Film fluorescence spectra: A – chitosan film modified with PVA and CTAB; B – chitosan film modified with PVA; C – chitosan film.

The system of vibrational levels of the pyrene molecule is sensitive to the properties of surrounding substances. In this regard, it is possible to use the method of fluorescent probes. Its essence is that luminescent molecules react to changes in the parameters of their microenvironment by changing the intensity of luminescence. This allows us to characterize the microenvironment around the probe molecules and evaluate their parameters that affect the luminescence of the probe [21].

In this case, the pyrene is a luminescent probe that shows the polarity of the microenvironment of molecules by means of ratio to the intensities of the first and third maxima of the fluorescence spectrum (I_1/I_3). This value can be used to estimate the sorption ability of modified chitosan films and the effect of modifying substances on the intensity of pyrene fluorescence [19].

When the pyrene is sorbed from the DMSO solution to chitosan films, the polarity index decreases from 1.81 for the solution (Fig. 4, curve 0), up to 1.32 for chitosan film (Fig. 3, curve C) and up to 1.08 for chitosan film with the addition of CTAB (Fig. 3, curve A). The results are shown in Table 1. This indicates that the modified matrices are more hydrophobic than the unmodified matrices and they represent a good basis for the luminescent signal.

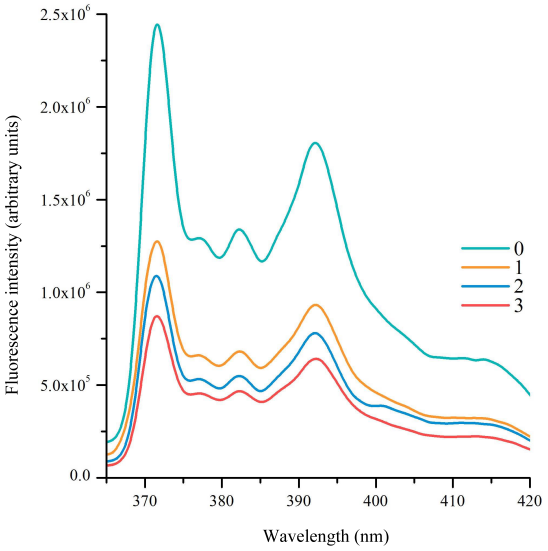


Fig. 4 Fluorescence spectra of solutions: 0 – initial solution; 1 – after static sorption (t = 30 min) with chitosan film; 2 – after static sorption (t = 30 min) with chitosan-PVA film; 3 – after static sorption (t = 30 min) with chitosan-PVA-CTAB film.

Table 1 Indexes of polarity.

	Films type	Index of polarity, units
A	Chitosan, PVA, CTAB	1.08 ± 0.03
B	Chitosan, PVA	1.21 ± 0.04
C	Chitosan	1.32 ± 0.04
0	DMSO-solution	1.81 ± 0.05

Reliability and reproducibility of results of pyrene determination by SPL are confirmed by the calculations of extent of pyrene extraction at static sorption from initial solution. Fluorescence spectra of the initial and final samples of DMSO and pyrene solutions (before

and after pyrene sorption) were measured to calculate the extent of pyrene extraction by the films. The results of solution analysis are shown in Fig. 4. The most effective matrix was modified PVA and CTAB and its extent of extraction was 64%.

In Ref. [2], films of chitosan, cellulose and cellulose diacetate were made. The degree of pyrene extraction by these matrices was respectively 4, 24, and 15%. The pyrene polarity indexes were respectively 1.22 ± 0.02, 1.23 ± 0.01 and 1.51 ± 0.02. The analysis of pyrene fluorescence spectra on matrices after sorption from a water-ethanol solutions demonstrated that the intensity of pyrene fluorescence is low, and the sorption capacity of matrices from cellulose diacetate and chitosan from a water-ethanol solution of pyrene is low. Similar results were presented by the authors in Refs. [22–23], where the value of the polarity index varied from 1.72 to 1.32 for different types of matrices.

In this work, the modification of chitosan films was carried out with PVA and CTAB. Based on the results of fluorescent analysis of pyrene in an aqueous solution of DMSO, it can be concluded the sorption capacity of the films significantly increases. The pyrene recovery rate on modified solid matrices was 64%, which is more than in the presented literature data [2, 22–23]. The pyrene polarity index decreased to 1.08 ± 0.03, compared to 1.81 ± 0.05 in the initial DMSO solution, indicating greater hydrophobicity of the modified matrices. Thus, the using of the proposed solid matrices for TFL is enough effective.

The extent of pyrene extraction was calculated by Eq. (1):

$$R = \frac{I_{sol} - I_{film}}{I_{sol}} \times 100\%, \qquad (1)$$

where I_{sol} is maximum luminescence intensity of the initial solution; I_{film} is maximum intensity of solution luminescence after static film sorption.

The results of the calculations are shown in Table 2.

Table 2 Extent of pyrene extraction by films.

	Solutions after film sorption	Extent of pyrene extraction from solution by films, %
1	Chitosan	48 ± 2
2	Chitosan, PVA	53 ± 3
3	Chitosan, PVA, CTAB	64 ± 4

For the most effective modification of the matrices, graphs (Fig. 5) of dependence of the pyrene fluorescence intensity on the amount of CTAB at three pyrene concentrations: 10^{-5}, 10^{-6} and 10^{-7} were plotted. From the obtained graphs, it can be seen that when pyrene is sorbed from the DMSO solution onto a matrix modified by CTAB and PVA, the intensity of pyrene fluorescence increases significantly with an increase in the amount of CTAB in the film composition. The maximum values of pyrene fluorescence on the modified film are observed at the mass fraction of CTAB $\omega = 15 \times 10^{-3}$ %. With further addition of CTAB, the pyrene fluorescence signal does not increase. Thus, it is advisable to use this amount of CTAB for effective analysis of pyrene using solid chitosan matrices.

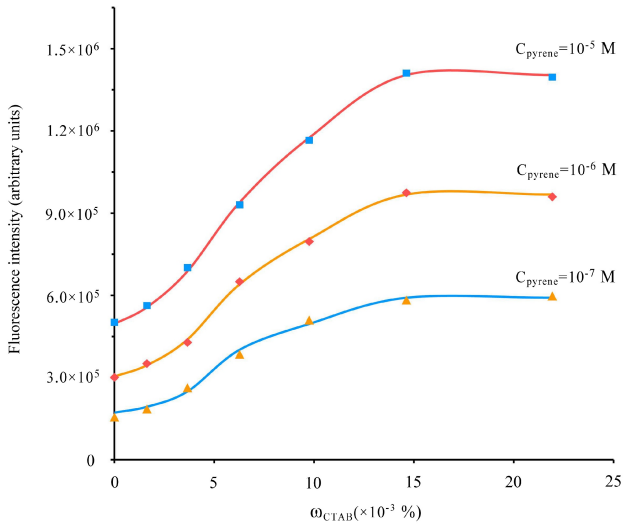


Fig. 5 Dependence of fluorescence intensity pyrene on chitosan-PVA-CTAB films on mass fraction CTAB.

These results can be explained by the fact that the polymer structure changes when PVA and CTAB are added to the chitosan solution. When biopolymers (chitosan) are mixed with synthetic polymers (PVA), new composite materials with new characteristics are formed. The modified chitosan film with PVA combines the properties of both polymers because hydrogen bonds are formed between the OH- and NH- chitosan groups and the OH- group at PVA. [24]

It is also known from the literature that chitosan is quite effective in forming complexes with surfactants. Chitosan is cationic biopolymer, and at addition of molecules to it anion surfactant, it forms strong communications due to Coulomb interaction [25].

At the same time, it loses charge, and the formed complex ceases to be soluble in water and precipitates. In our research when anionic surfactant was added, strong enough chitosan films failed to synthesize.

The addition of a cationic surfactant is also produced complexes that strongly alter the initial structure of the polymer chain and the physical properties of the polymer. The type of change depends on the ratio of polymer to surfactant concentrations. Complexes with whole micelles can be formed at micelle-forming surfactant concentrations higher than critical micelle formation concentration [26].

It can be assumed that CTAB molecules and micelles attach to the chitosan polymer chain and the matrix becomes more porous with more hydrophobic

bonds, whereby pyrene attachment occurs more efficiently.

4 Conclusion

The results confirm the high solubilizing ability of solid matrices based on chitosan and allow using the hydrophobic properties of chitosan films in hydrophobic form for pyrene analysis. It was found that SPL analysis allows increasing the sensitivity of pyrene detection in aqueous media without additional extraction of substances and concentration with organic solvents. Also, when using solid matrices, it is possible to perform a luminescent analysis of substances with a large range of optical transparency.

The study of the spectral characteristics of the pyrene luminescent probe suggests that in films with CTAB, hydrophobic pyrene molecules are in a solubilized state inside micelles. Studying the parameters of pyrene adsorption from aqueous DMSO solutions allows us to conclude that pyrene molecules are sorbed on a solid matrix inside CTAB associates. Modification of chitosan matrices using PVA and CTAB allows us to increase the efficiency of concentration of pyrene molecules. Therefore, this allows improving the analytical characteristics of the luminescent pyrene detection method.

Further studies suggest using the results obtained for the quantitative determination of pyrene with the use of SPL with modified chitosan matrices in aqueous environment and food items. Also the results can be used to develop a method for determining other types of PAHs, such as BP, for using in test systems for environmental monitoring.

Disclosures

All authors declare that there is no conflict of interests in this paper.

References

1. H. I. Abdel-Shafy, M. S. M. Mansour, "A review on polycyclic aromatic hydrocarbons: Source, environmental impact, effect on human health and remediation", Egyptian Journal of Petroleum 25(1), 107–123 (2016).
2. A. V. Strashko, Razrabotka polisakharidnykh matrits i usloviy tverdofaznogo lyuminestsentnogo opredeleniya politsiklicheskikh aromaticheskikh uglevodorodov dlya ekologicheskogo monitoringa vodnykh sred, Dissertation, Saratov State University, 124 p. (2015) [in Russian].
3. K.-H. Kim, S. A. Jahan, E. Kabir, and R. J. C. Brown, "A review of airborne polycyclic aromatic hydrocarbons (PAHs) and their human health effects", Environment International 60, 71–80 (2013).
4. A. Ramesh, A. Archibong, D. Hood, Z. Guo, and B. Loganathan, "Global Environmental Distribution and Human Health Effects of Polycyclic Aromatic Hydrocarbons" Chapter in Global Contamination Trends of Persistent Organic Chemicals, 97–126 (2011).
5. "Maximum permissible concentrations of pollutants in the atmospheric air of urban and rural settlements", Resolution of the Government of the Russian Federation No. 165 on the approval of hygienic standards of the GN 2.1.6.3492-17, Amendment of 31.05.2018 [in Russian].
6. "About food safety", Technical Regulations of the Customs Union, 127–152 (2011) [in Russian].
7. S. R. Sokolnikova, D. A. Tatarinov, and N. A. Myslitskaya, "Change of luminescent properties of pyrene in surface-active substance solution using an albumin", Memoirs of the Faculty of Physics 4, 1941101 (2019) [in Russian].
8. S. M. Rogacheva, A. B. Shipovskaya, A. V. Strashko, T. I. Gubina, E. V. Volkova, and A. G. Melnikov, "Polysaccharide fibers as matrices for solid-surface fluorescence", International Journal of Polymer Science 2014, 183413 (2014).
9. D. A. Tatarinov, S. R. Sokolnikova, and N. A. Myslitskaya, "Influence of silver nanoparticles on the luminescent properties of pyrene in micellar solution", Electronic, spin and quantum processes in molecular and crystal systems: Theses of reports and presentations, BGPU, Ufa, 21 (2019) [in Russian].
10. T. Saitoh, H. Itoh, and M. Hiraide, "Admicelle–enhanced synchronous fluorescence spectrometry for the selective determination of polycyclic aromatic hydrocarbons in water", Talanta 79, 177–182 (2009).
11. W. B. Wilson, A. A. Costa, H. Wang, A. D. Campiglia, J. A. Dias, and S. C. L. Dias, "Preconcentration of water samples with BEA zeolite for direct determination of polycyclic aromatic hydrocarbons with laser-excited timeresolved Shpol'skii spectroscopy", Microchemical Journal 110, 246–255 (2013).
12. A. H. Ackerman, R. J. Hurtubise, "Methods for coating filter paper for solid-phase microextraction with luminescence detection and characterization of the coated filter paper by infrared spectrometry", Analytical Chemical Acta 474(1–2), 77–89 (2002).
13. A. I. Suvorova, A. L. Suvovrov, M. V. Ivanenko, and E. I. Shishkin, "Nanocomposite membrane films based on cellulose ethers and tetraethoxysilane", Russian Nanotechnologies 4(1–2), 154–161 (2009) [in Russian].
14. M. Rinaudo, "Chitin and chitosan: properties and applications", Progress in Polymer Science 31(7), 603–632 (2006).

15. V. F. Adulin, “Technology and properties of chitosan from the river cancer shell”, Journal of SGTU 4(16), 18–24 (2006) [in Russian].
16. M. Jabli, H. V. Baouab, M. S. Roudesli, and A. Bartegi, “Adsorption of acid dyes from aqueous solution on a chitosan-cotton composite material prepared by a new pad-dry process”, Journal of Engineered Fibers and Fabrics 6(3), 1–12 (2011).
17. HORIBA Instruments Incorporated. Fluorolog-3 Operation Manual rev. (2014).
18. L. A. Currie, G. Svehla, “Nomenclature for the presentation of results of chemical analysis. (IUPAC Recommendations 1994)”, Pure and Applied Chemistry 66(3), 595–608 (1994).
19. G. V. Mel’nikov, T. I. Gubina, and O. A. Dyachuk, “Influence of the polarity of the microenvironment of pyrene on the intensity of its solid-phase luminescence”, Russian Journal of Physical Chemistry 80(7), 1160–1163 (2006).
20. S. N. Shtykov, “Chemical analysis in nanoreactors: Main concepts and applications”, Journal of Analytical Chemistry 57(10), 859–868 (2002).
21. E. V. Naumova, A. G. Melnikov, and G. V. Melnikov, “Luminescence quenching by heavy metal ions of probes based on anthracene, pyrene, and eosin in human serum albumin”, Journal of Applied Spectroscopy 80(2), 159–163 (2013).
22. L. Chen, D. Chen, and C. Wu, “A New Approach for the Flocculation Mechanism of Chitosan”, Journal of Polymers and the Environment 11(3), 87–92 (2003).
23. L. Chen, D. Chen, and C. Wu, “Studying Flocculation Mechanism of Chitosan with Pyrene-fluorescence Probe Method”, Chinese Journal of Chemistry 21, 1224–1228 (2003).
24. K. Choo, Y. C. Ching, C. H. Chuah, S. Julai, and N.-S. Liou, “Preparation and characterization of polyvinyl alcohol-chitosan composite films reinforced with cellulose nanofiber”, Materials 9(8), 644 (2016).
25. M. Thongngam, D. J. McClements, “Characterization of Interactions between chitosan and an anionic surfactant”, Journal of Agricultural and Food Chemistry 52(4), 987−991 (2004).
26. K. N. Bakeev, E. A. Ponomarenko, T. V. Shishkanova, D. A. Tirrell, A. B. Zezin, and V. A. Kabanov, “Complexation of amphiphilic polyelectrolytes with surfactants of the same charge in water solutions”, Macromolecules 28(8), 2886−2892 (1995).

Electrical Properties of Porous Silicon as a Biosensor Material

Kristina A. Ganichkina* and Natalia V. Latukhina
Department of Solid State Physics and Nonequilibrium Systems, Samara National Research University, 34 Moskovskoe shosse, Samara 443086, Russian Federation

*** e-mail:** ganichkina.k@mail.ru

Abstract. The electrical properties of porous silicon nanocomposites with various glucose solutions were studied. The current-voltage characteristics (I–V) of glucose solutions in water and tear fluid, as well as porous silicon samples of various porosities saturated with these solutions were measured. The porosity and glucose content in the pores were determined by the gravimetric method. Measurements of the I–V characteristics and photoconductivity of nanocomposites showed that their electrical conductivity appreciably depends on the glucose content in solutions. © 2020 Journal of Biomedical Photonics & Engineering.

Keywords: glucose; porous silicon; PC; por-Si; nanocomposite; biosensor; CVC; photoconductivity.

Paper #3348 received 17 Jan 2020; revised manuscript received 11 Mar 2020; accepted for publication 11 Mar 2020; published online 26 Mar 2020. doi: 10.18287/JBPE20.06.010306.

1 Introduction

The problem of the choice of material for creating biosensors is relevant today. New materials are still being researched for use as a sensitive layer. It is important to solve such problems as a high sensitivity of the material to the studied object, selectivity, non-toxicity of biomaterial, biocompatibility. Porous silicon is a promising material for the creation of biosensors. Due to the developed surface of porous silicon, it can be used as a biosensitive layer [1, 2].

The widespread use of porous silicon for medical purposes makes the problem of the dependence of the physicochemical properties of nanocomposites based on porous silicon on their structure and composition very urgent. Thus, the development of methods for studying these properties is important.

When creating biosensors on porous silicon, it is promising to use its electrical properties. The electrical properties of porous silicon are highly dependent on substances trapped in the pores [6, 7]. This is primarily due to the presence of nanocrystals on the pore walls, the electronic structure of which is very sensitive to the presence of impurities in the pores. Hence, this is a possibility of detecting substances by changing the electrical properties of porous silicon [8].

In this paper, we studied the dependence of the electrical conductivity of porous silicon on the content of glucose solutions in it with different concentrations of matter. The choice of glucose as a test substance is due to the relevance of improving methods for analyzing blood glucose levels. This analysis is very important for people with diabetes. It is important for a person suffering from diabetes to know the level of glucose for control, diet and drug treatment [1].

2 Experimental and Calculation Methods

2.1. Sample manufacturing procedure

Samples of porous silicon were prepared by electrochemical etching in a fluorine-containing solution. The composition of the electrolyte: water, isopropyl alcohol, hydrofluoric acid in a ratio of 6:9:5: $H_2O + (CH_3)_2CHOH + HF$.

Etching occurred at currents of 60 mA, 80 mA and lasted for 15, 20 and 30 min (Fig 1). Porosity was determined by the gravimetric method from the decrease in sample weight after etching. Depending on the etching conditions, the porosity varied from 17% to 43%. Italics show the values of porosity calculated for other samples made by similar methods. The accuracy of the calculation of porosity by the gravimetric method is determined by the accuracy of weighing and determining the geometric parameters of the porous

Table 1 Samples and etching conditions.

Sample #	Surface type	Etching mode		Porosity, % (expected)
		I, mA	Etching time, min	
Y	Polished surface	80	15	***17***
O	Polished surface	80	10	***17***
U	Polished surface	80	20	***17***
G	Polished surface	60	20	17
X	Polished surface	80	30	22
E	Polished surface	60	30	34
R	Polished surface	80	30	***34***
A	Polished surface	60	20	***17***
K	Textured surface	80	30	37
P	Textured surface	80	15	21
Z	Textured surface	60	20	***21***
L	Textured surface	80	20	***21***
H	Textured surface	60	15	***21***
№1	Textured surface	60	10	***21***
№2	Textured surface	60	30	***37***
J	Ground surface	80	20	***43***
N	Ground surface	60	20	***43***

layer and does not exceed 0.3%, however, the difference in the values of porosity of identical samples reaches units of percent that is explained by the influence of uncontrolled factors of the etching process [3]. Therefore, the numerical values of porosity shown in Table 1 are estimated. Nevertheless, from an analysis of these data, it can be concluded that the samples with a polished surface have the maximum porosity (43%); therefore, they are most promising for creating a biosensor.

To create nanocomposites with porous silicon, substances such as glucose and saline were used to understand how the properties of the material change when these substances are present in the pores because both substances are present in human blood and plasma in a noticeable amount. Solutions of glucose in the lacrimal fluid were also investigated because a number of researchers propose a method for determining the sugar content in human blood by the study of tears.

On samples X, O, G (polished surface); L, K (textured surface) and N (ground surface) and discrete contacts were applied through a mask with a conductive paste, and the I–V characteristics were measured on three parts of the sample: porous silicon, part with a glucose solution of different concentrations in water, part with a glucose solution of different concentrations in lacrimal fluid. Previous studies of the IR spectra of nanocomposites showed that the porous layer can be saturated with glucose from aqueous solutions [4].

2.2. Measurement of photoconductivity and CVC

A stand to measure photoconductivity and current-voltage characteristics (Fig. 1) was used.



Fig. 1 Stand for measuring the current-voltage characteristic.

In this paper, to measure the dark current, the sample was fixed on a special holder and placed in a lightproof casing. To record the light characteristics, the sample was illuminated with a lamp. The current flowing through the sample was measured with a V7-21A universal voltmeter. A stabilized voltage was also supplied from the B5-43 power source. The voltage was measured with a V7-26 universal voltmeter; its measurement accuracy was 0.1 mV.

The resistance of the samples was calculated by measuring the voltage and current flowing through the sample.

To calculate the resistivity and conductivity, we use the formulas:

$$\rho = \frac{R \times d \times h}{L}, \quad (1)$$

$$\sigma = \frac{1}{\rho}, \quad (2)$$

where R – the resistance, d – the thickness of the plate, we take it equal to 1, L – the distance between the contacts, h – contact length (Fig. 2).

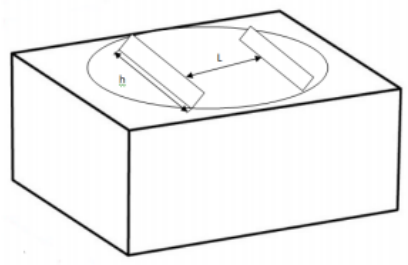


Fig. 2 Scheme for calculating the resistivity.

To measure the I–V characteristics, solutions of glucose in water containing 1%, 2%, 3%, and 4% of the substance were prepared, and glucose solutions in the Slezin pharmacy preparation containing 3%, 6%, and 12% glucose. Then, the current-voltage characteristics were measured and the electrical resistances of glucose, silicon, and then glucose together with silicon were calculated, and the relative measurement error ΔR/R was also calculated.

Researchers Yihao Chen, Siyuan Lu et al. developed the biosensor as a "two-electrode system" (working electrode and counter electrode) in measurements *in vivo*. A clinical study was conducted *in vivo* by examining the presence of glucose in tissue fluid. The work presents the electrochemical and mechanical characteristics of the device, as well as the amperometric I–t result recorded by a biosensor attached to the skin surface [5].

3 Results

Based on the experiment, the I–V curves of the samples were constructed in the absence and presence of glucose (Fig. 3). The figures show graphs for a glucose solution (1% glucose solution in water), for a porous silicon wafer (por-Si) and for a nanocomposite (por-Si and an aqueous glucose solution of various concentrations).

It can be seen from the graphs in Fig. 3 for the most part, the dependence of current on voltage is linear in nature that allows us to use these data to calculate the resistance.

According to the results of measurements and calculations, a final Table 2 was compiled of the dependence of the resistance of the PC samples on the glucose content in them.

Based on the results, a graph of the dependence of the sample resistance on the percentage glucose in the solution was constructed (Fig. 4).

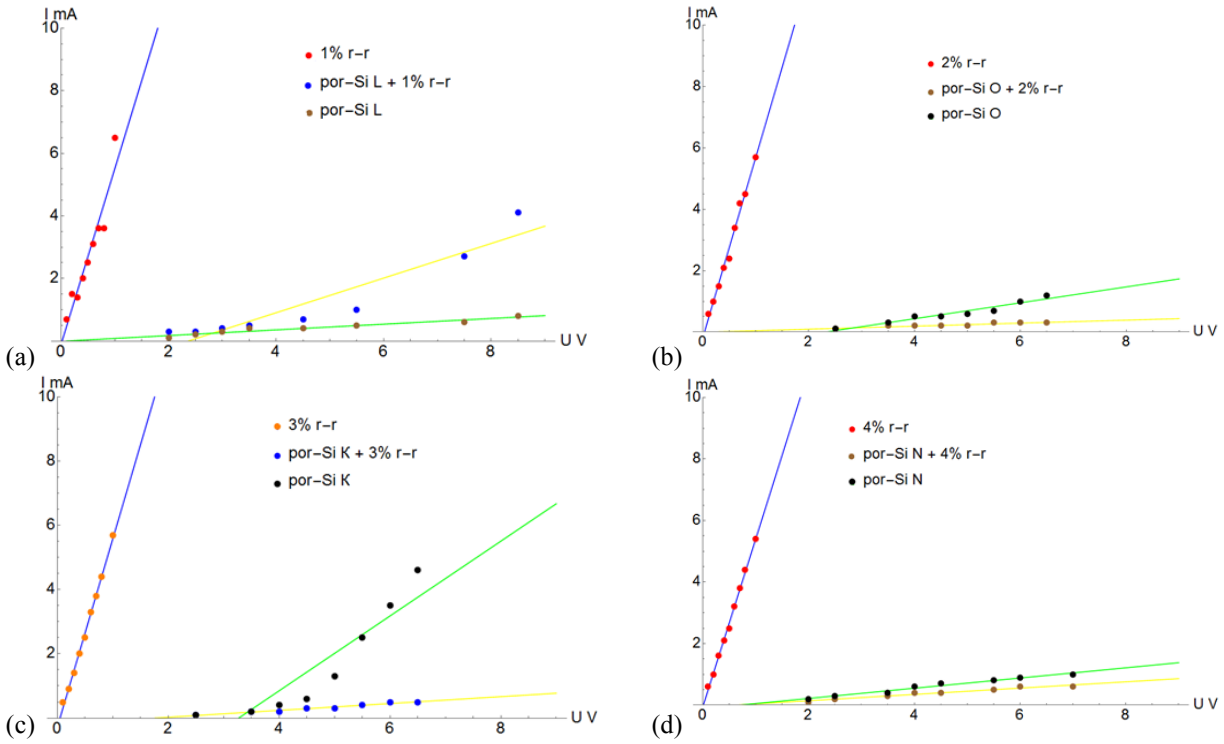


Fig. 3 CVC of the studied samples: (a) 1%, (b) 2%, (c) 3%, (d) 4% glucose.

Table 2 Dependence of the resistance of PC samples on glucose content.

Sample number and glucose concentration	R glucose, kOhm	ΔR/R glucose, %	R por-Si, kOhm	ΔR/R por-Si, %	R glucose + por-Si, kOhm	ΔR/R glucose + por-Si, %
L (1%)	178.4	3.4	13222.5	14	4285.7	1.9
O (2%)	181.7	1.5	10552.5	7.2	6431.2	17.4
K (3%)	191.4	3.6	12756.2	11	1728.2	1.6
N (4%)	186.8	1.2	8737.5	9.1	1209.1	22.6

As can be seen from the graph in Fig. 4, the resistance of the nanocomposite significantly depends on the concentration of glucose in the solution.

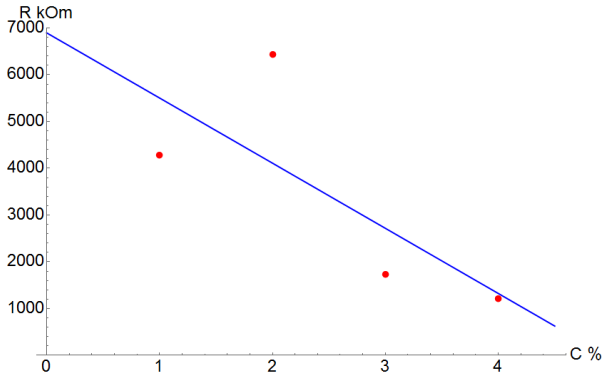


Fig. 4 The dependence of the silicon nanocomposite + glucose resistance on the percentage of glucose in the solution.

The next series of studies was related to measuring the dependence of the resistance of a silicon + glucose nanocomposite on the percentage of glucose in the tear fluid (3%, 6%, and 12% glucose). Porous silicon, on which nothing was applied, was taken as a control sample. The figures show graphs separately for the por-Si nanocomposite + glucose solution with the addition of a tear (1% glucose solution in a tear), for a porous silicon wafer (por-Si) and for a nanocomposite (por-Si and an aqueous glucose solution of various concentrations).

A porous silicon sample with added solutions of various concentrations was used. Also, according to the results, a graph of the dependence of the resistance of the silicon + glucose nanocomposite on the percentage of glucose in the solution was built. Based on the results of measurements and calculations, a final Table 3 of the dependence of the resistance of PC samples on the presence of a certain amount of glucose in them was compiled.

Figs. 5 and 6 show the I–V characteristics and the dependence of resistance, measured and calculated similarly to the previous ones (Figs. 3–4).

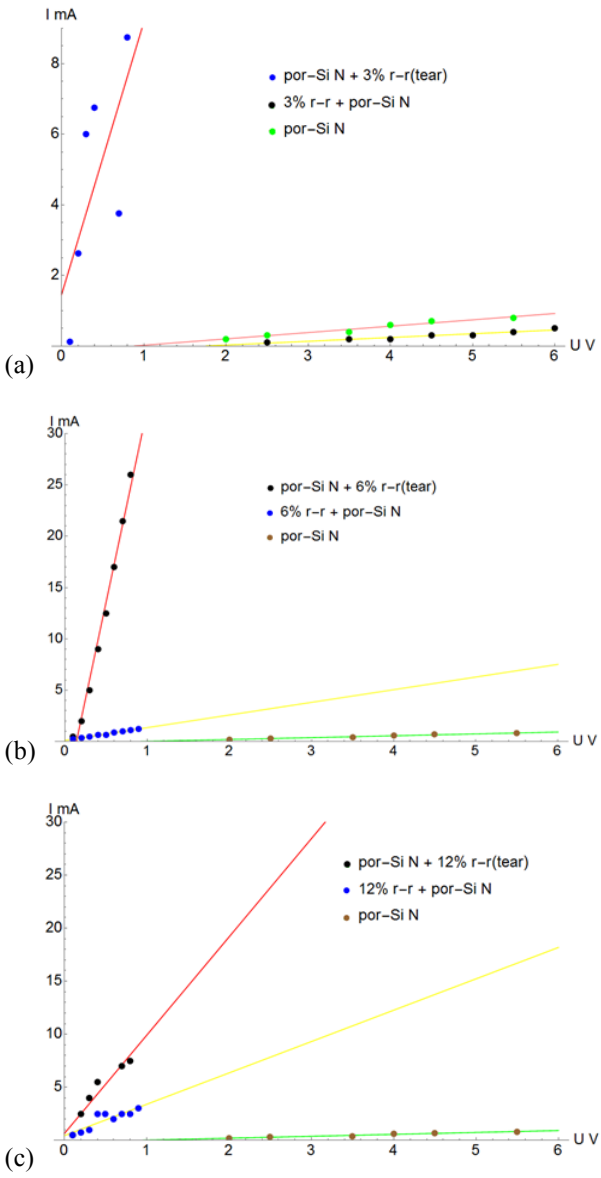


Fig. 5 CVC of a silicon + glucose nanocomposite of the percentage glucose in the tear fluid (3%, 6%, and 12% glucose).

Table 3 Dependence of the stability of PC samples on the presence in them of a certain amount of glucose.

Sample number and glucose concentration	R glucose + tear, kOhm	ΔR/ R glucose + tear, %	R por-Si, kOhm	ΔR/ R por-Si, %	R glucose + tear + por-Si, kOhm	ΔR/ R glucose + tear + por-Si, %
N (3%)	783.45	0.3			11260	4.8
N (6%)	597.77	0.4	8737.5	3.5	21250	5.1
N (12%)	380.13	1.4			9990	3.2

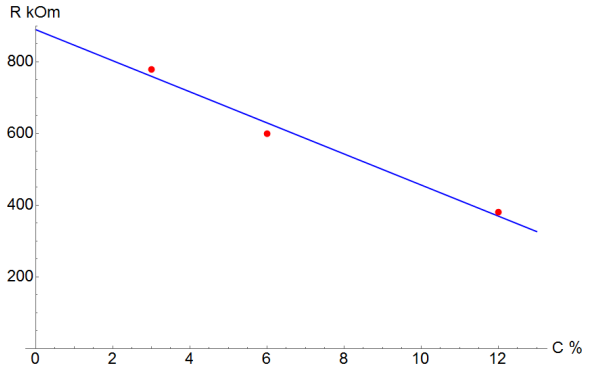


Fig. 6 The dependence of the silicon nanocomposite + glucose resistance on the percentage of glucose in the tear fluid.

Table 4 Calculation of dark characteristics: resistivity and conductivity.

Sample	p_t, Ohm per square	σ_t, $Om^{-1}\cdot$ per square
G	$1.661\cdot10^{7}$	$6.020\cdot10^{-8}$
G+NaCl	$1.351\cdot10^{7}$	$7.404\cdot10^{-8}$
X – control sample	$8.365\cdot10^{6}$	$1.196\cdot10^{-7}$
X+6% glucose solution	$4.350\cdot10^{6}$	$2.299\cdot10^{-7}$
X+12% glucose solution	$4.021\cdot10^{6}$	$2.487\cdot10^{-7}$

Table 5 Calculation of light characteristics: resistivity and conductivity.

Sample	p_{sv}, Ohm$\cdot$ per square	σ_{sv}, $Ohm^{-1}\cdot$ per square
G	$5.830\cdot10^{5}$	$1.715\cdot10^{-6}$
G+NaCl	$3.250\cdot10^{5}$	$3.077\cdot10^{-6}$
X – control sample	$1.239\cdot10^{6}$	$8.070\cdot10^{-7}$
X+6% glucose solution	$4.35\cdot10^{5}$	$2.299\cdot10^{-6}$
X+12% glucose solution	$1.428\cdot10^{6}$	$7.003\cdot10^{-7}$

As can be seen from the graph in Fig. 6, the resistance of the silicon + glucose nanocomposite depends on the concentration of glucose in the lacrimal fluid. This dependence is rather well approximated by a decreasing linear function. For a nanocomposite with an aqueous glucose solution, the function is also diminishing, although its linearity is not so obvious.

For various samples of porous silicon with various supported substances (NaCl; 6%, 12% glucose solutions), photoconductivity was measured. By measuring the current – voltage characteristics with and without illumination, it is possible to determine the dark (σ_t) and light (σ_{sv}) conductivities of the samples, as well as $\Delta\sigma = \sigma_t$ (PC) – σ_t (PC + substance), $\Delta\sigma/\sigma_t$, and $\Delta\sigma/\sigma_{sv}$. Fig. 7 shows the I–V characteristics of a nanocomposite with NaCl.

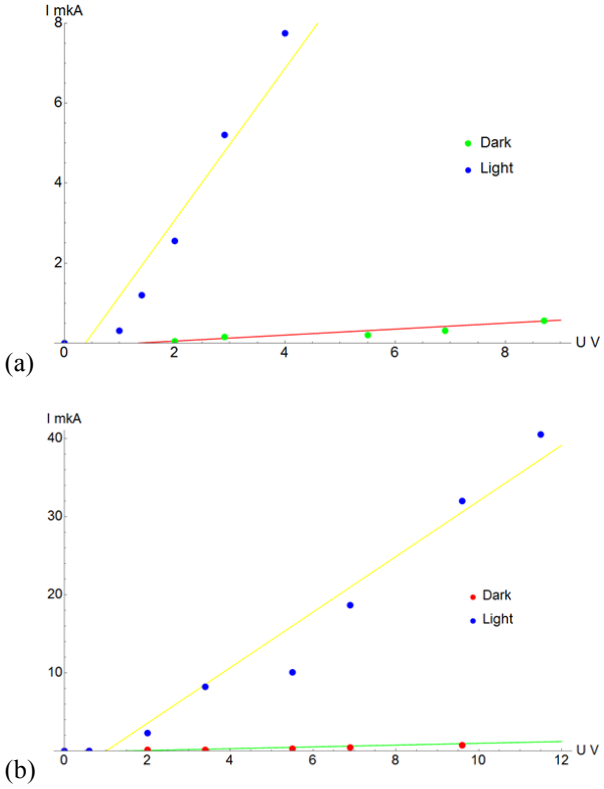
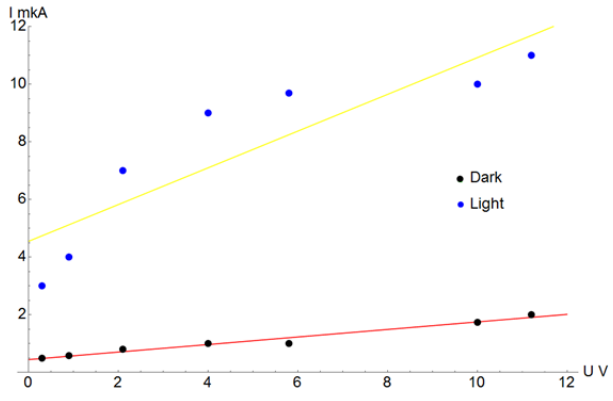
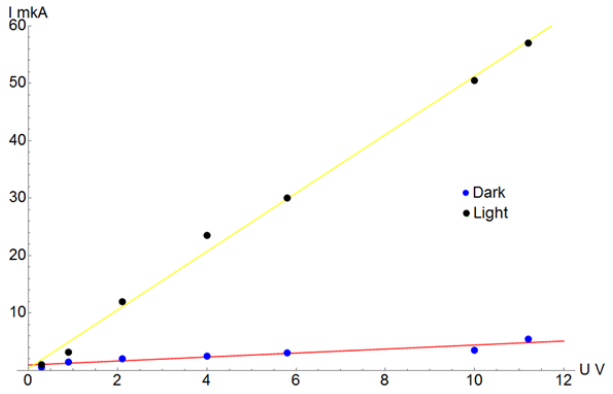


Fig. 7 CVC: (a) sample G-control and (b) sample G + NaCl.

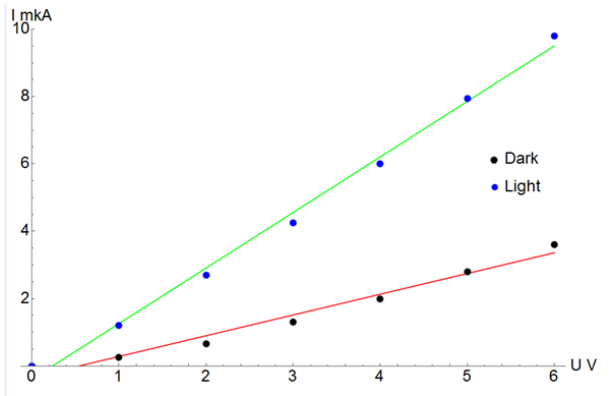
Fig. 8 shows the I–V characteristics of a nanocomposite with 6 and 12% glucose.



(a)



(b)



(c)

Fig. 8 CVC: (a) X – control sample, (b) X with glucose of 6% solution, (c) X with glucose of 12% solution.

The calculation of resistivity and conductivity is given in Tables 4–5.

The obtained results demonstrate that all plates have high photosensitivity. The presence of glucose on the porous layer shows a significant increase in both dark and light conductivity. The presence of NaCl in the sample does not significantly change the conductivity; the order remains the same. Calculations of the change in dark conductivity with the addition of substances to the samples are shown in Table 6.

Table 6 Change in dark conductivity with the addition of substances to the samples.

№ sample	$\Delta\sigma/\sigma_t$, %	$\Delta\sigma/\sigma_{sv}$, %	Amount of substance
G (with NaCl solution)	23	82	0.016
X (when adding 6% glucose solution in water)	92	188	0.323
X (when adding 12% glucose solution in water	120	14	0.571

4 Conclusion

It was found that the resistance of porous silicon varies markedly in the presence of glucose in the pores. With an increase in glucose content, the resistance markedly decreased for all the studied samples with different porosities. Samples with a porous layer made on a polished surface (N) have the highest porosity that is an attractive quality for using such a material in a biosensor. In this case, a nanocomposite with such a surface is characterized by a linear dependence of the resistance on the glucose content in the pores. From this, we can conclude that porous silicon is a promising material for creating an electric or combined optical-electric glucose biosensor.

Disclosures

All authors declare that there is no conflict of interests in this paper.

References

1. A. Samuilkina, "New biosensors measure sugar levels with a few drops of sweat," High-tech, 2016 (accessed 10 august 2019).
2. O. I. Ksenofontova, A. V. Vasin, V. V. Egorov, A. V. Bobyl', F. Y. Soldatenkov, E. I. Terukov, V. P. Ulin, N. V. Ulin, and O. I. Kiselev, "Porous silicon and its applications in biology and medicine," Technical Physics 59(1), 66–77 (2014).

3. N. V. Latukhina, D. A. Lizunkova, I. A. Shishkin, G. A. Rogozhina, and V. A. Gurenkova, "The influence of uncontrolled factors on the properties of porous silicon," Collection of reports of the VIII International Scientific Conference, 63–65 (2018).
4. K. A. Ganichkina, N. V. Latukhina, and D. R. Suyundukova, "Optical methods for studying porous silicon-based biomaterial," Proceeding of XVI All-Russian Youth Samara Competition – a conference of scientific papers on optics and laser physics, 268–276 (2018). [in Russian]
5. Y. Chen, S. Lu, S. Zhang, Y. Li, Z. Qu, Y. Chen, B. Lu, X. Wang, and X. Feng, "Skin-like biosensor system via electrochemical channels for noninvasive blood glucose monitoring," Science advances 3(12), e1701629 (2017).
6. S. Zairi, C. Martelet, N. Jaffrezic-Renault, R. M'gaïeth, H. Maâref, and R. Lamartine, "Porous silicon a transducer material for a high-sensitive (bio) chemical sensor: effect of a porosity, pores morphologies and a large surface area on a sensitivity," Thin Solid Films 383(1–2), 325–327 (2001).
7. W. Y. Tong, M. J. Sweetman, E. R. Marzouk, C. Fraser, T. Kuchel, and N. H. Voelcker, "Towards a subcutaneous optical biosensor based on thermally hydrocarbonised porous silicon," Biomaterials 74, 217–230 (2016).
8. J. Salonen, V. P. Lehto, "Fabrication and chemical surface modification of mesoporous silicon for biomedical applications," Chemical Engineering Journal 137(1), 162–172 (2008).

Studies of Red Blood Cell Aggregation and Blood Oxygenation on the Basis of the Optoacoustic Effect in Biological Media

Denis A. Kravchuk* and Ksenia A. Voronina**
Southern Federal University, 2 Shevchenko str., Building E, Taganrog 347922, Russian Federation

***e-mail:** kravchukda@sfedu.ru

****e-mail:** kususha-voronina@yandex.ru

Abstract. The most important task in the field of medical diagnostics is the creation and application of new diagnostic tools and methods, as well as diagnosis of physiological processes. To solve this problem, one may use the optoacoustic (OA) effect – thermooptical excitation of acoustic waves in a liquid medium under laser radiation absorption. This study utilizes numerical methods for modeling processes of oxygen saturation and red blood cells aggregation in the blood. Models of oxygenated red blood cells and their distribution in the blood are constructed using the Monte Carlo method. The acoustic signal from oxygenated and deoxygenated red blood cells was simulated at various levels of oxygen saturation. It was found that the level of spectral power density of the acoustic signal varies significantly and allows one to estimate the percentage of oxygen saturation of red blood cells in the blood with implementation of OA method. A model for the aggregation of red blood cells, combining red blood cells into clusters by hexagonal packing, was developed to increase compactness. It was found that using the OA method, it is possible to determine the level of red blood cells aggregation and of hematocrit level. © 2020 Journal of Biomedical Photonics & Engineering.

Keywords: photoacoustic effect; the level of red blood cells aggregation; Monte Carlo method; spherical source.

Paper #3355 received 26 Feb 2020; revised manuscript received 17 Mar 2020; accepted for publication 21 Mar 2020; published online 27 Mar 2020. doi: 10.18287/JBPE20.06.010307.

1 Introduction

In the conditions of development and improvement of medicine, it becomes necessary to develop and study new diagnostic methods, one of which is the optoacoustic (OA) effect. A numerical analysis of the optical characteristics of biological media provides necessary information for effective diagnosis. Modern methods for determining the optical characteristics of biological media require implementation of *in vitro* analysis, i.e. determination of attenuation by spectrophotometry, fluorescence spectroscopy, Raman spectroscopy, etc. [1]. The advantages of OA method during *in vivo* analysis reduce the time for deciding on the treatment method. There are numerous possibilities for studying blood composition *in vitro*, but non-invasive analysis is of great interest as it is a convenient and comfortable method that does not change the morphological composition of the blood [2].

Establishing the level of aggregation of red blood cells (AE) in the blood is important in the diagnosis of blood. Red blood cell aggregation requires clinical diagnosis; AE growth may lead to the development of diseases such as diabetes mellitus, hypertension, anemia, inflammation, etc. [3, 4]. In addition, the increase in aggregation may occur as a result of "side effects" of medications and may lead to blockade of small vessels by aggregates, and difficulties in transporting oxygen in human blood. In this regard, the analysis of aggregation level and oxygen saturation must be carried out for patients undergoing treatment in medical institutions [5–7]. To measure the level of red blood cell aggregation and oxygen saturation in the

blood, non-invasive techniques, for example utilizing AO effect, are needed. In order to do this, it is necessary to conduct research utilizing mathematical modeling. The authors in Ref. [8] performed mathematical modeling of the formation of OA signal from red blood cells without taking into account a backscattering signal. The authors of Ref. [9] performed optical diagnostics of tissues and their visualization. The authors carried out theoretical and experimental studies of AO signal with laser excitation [10]; they conducted experimental studies of AO effect in model suspensions in the presence of nanotubes and nanofibers without red blood cells modeling.

The aim of the work is the modeling of red blood cells considering oxygen saturation using the Monte Carlo method, development of a mathematical model of red blood cell aggregation by hexagonal packing, and calculation of acoustic signals generated as a result of OA conversion from red blood cells to establish the possibility of aggregation level and oxygen saturation estimation.

2 Materials and Methods

A workflow of OA imaging consists in detecting broadband ultrasonic signals generated in biological mediums by laser radiation absorbing. The advantage of the method, in contrast to the methods of radiography and computed tomography, is the application of low-energy photons and ultrasonic waves.

Ultrasonic wave in biological tissues allows obtaining an improved signal-to-noise ratio and high spatial resolution in deep tissues with high contrast. Spatial resolution is determined by ultrasonic focal power and ultrasonic passband. Biological tissues contain up to 70% of water, therefore, the distribution of the OA signal will be considered like that in water. When using the OA effect, tissues are irradiated with a laser using short pulses (with a duration of several nanoseconds). The optical and thermoelastic properties of the tissue absorbing laser radiation are studied by recording acoustic pressure using ultrasonic transducers [11]. To enhance the signal, the use of nanosized agents is effective. Carbon nanotubes (up to 100 nm in size) strongly absorb laser radiation. This allows one to use low-power lasers to prevent skin damage [12–14].

In Refs. [15, 16] (mathematical models have described the formation of an OA signal from an erythrocyte model as a spherical absorption source) the authors concluded that the amplitude of the OA signal monotonically increases with an increase of red blood cells concentration, which makes it possible to determine the hemoglobin level. Thus, it is proposed to use the OA effect to establish the degree of red blood cells aggregation.

To solve the stated problems, it is proposed to use signal processing methods, system analysis, and mathematical statistics. In mathematical modeling, the Matlab R2014b environment has been used as a toolkit.

The geometry of the OA modeling is shown in Fig. 1. The red and blue filled circles are two types of OA sources with different absorption coefficients, occupying the laser-illuminated region.

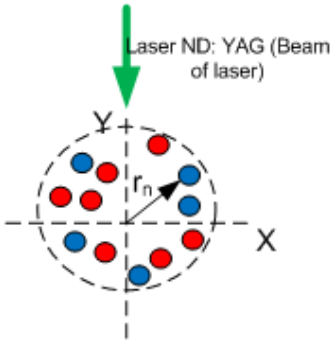


Fig. 1 Two types of acoustic signal sources (red – oxygenated red blood cells, and blue circles – deoxygenated red blood cells).

The analytical expression of the acoustic field formed by the liquid sphere may be written in the form of Eq. (1) [16]:

$$p_f^1(q) = \frac{i\mu\beta I_0 v_s \alpha^2}{C_p r} \frac{\left[\sin q - q\cos q\right] e^{ik_f(r-\alpha)}}{q^2\left[(1-q)\left(\frac{\sin q}{q}\right) - \cos q + i\rho v \sin q\right]}, \quad (1)$$

where μ is the absorption coefficient, C_P is isobaric specific heat, β is the coefficient of thermal expansion, α is the radius of the absorbing sphere, $\rho=\rho_s/\rho_f$ and $v=v_s/v_f$ are the dimensionless density and speed of sound (v_s is the speed of sound in red blood cells, v_f - the speed of sound in blood plasma), respectively.

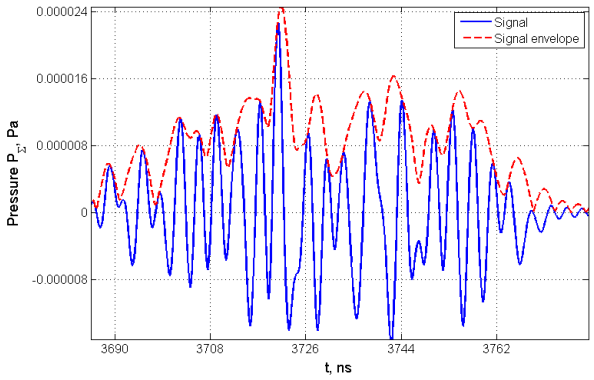


Fig. 2 Acoustic signal at 99% oxygen saturation (with signal envelope).

Fig. 2 shows the pressure curve of the acoustic signal for a simulated sample with saturation (SO_2 = 100%) while exposition with 1064 nm laser.

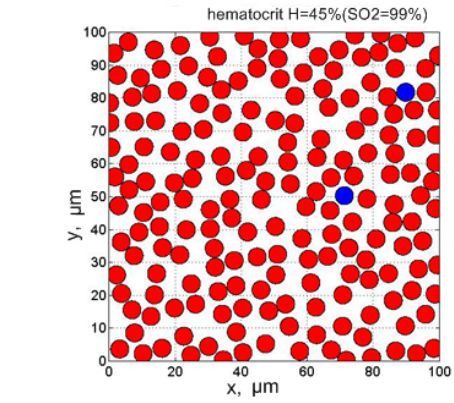
Mathematical modeling of oxygenated and deoxygenated erythrocytes consists in the formation of a three-dimensional realization of tissues with the condition of non-overlapping spheres representing simulated red blood cells in a volume of 100×100×100 μm^3. The simulated volume is filled with

red blood cells approximated in the form of liquid spheres with a hematocrit level of 40% since it is close to normal for human blood (Fig. 3). Moreover, in the model, oxygenated and deoxygenated red blood cells have certain densities, sound velocities, and absorption coefficients. Similarly, we form tissues with aggregated red blood cells (Fig. 4). In this case, we find the spatial positions of randomly distributed red blood cells within the study area of 100×100 μm^2. The number of clusters also determines the number of cells that could be attached to one cluster. The maximum packing density of red blood cells was achieved using hexagonal packing for each cluster [15, 18–20].

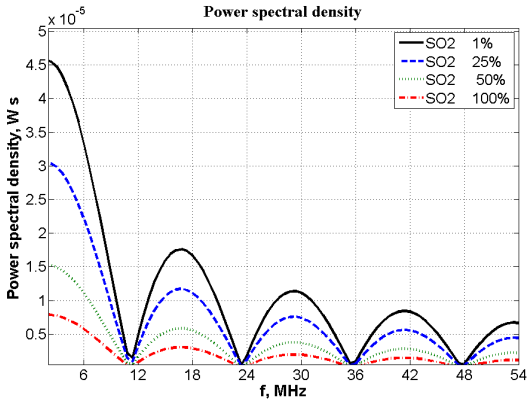
3 RESULTS

The model allows one the formation of red blood cells into aggregates with varying degrees of filling Fig. 4.

Fig. 3 shows the spectral power densities of the acoustic signal at 1%, 25%, 50%, and 100% of saturation. A large range of simulated levels of saturation is given in order to show the possibilities of the OA method for recording oxygen saturation. As the oxygen saturation of SO_2 increased, the spectral power of the signal also increased. An algorithm has been developed for modeling the implementation of 2D tissues, consisting of oxygenated red blood cells and deoxygenated red blood cells [15].



(a)



(b)

Fig. 3 (a) Randomly placed non-overlapping red blood cells simulating the implementation of 2D tissue, (b) spectral power density of the acoustic signal.

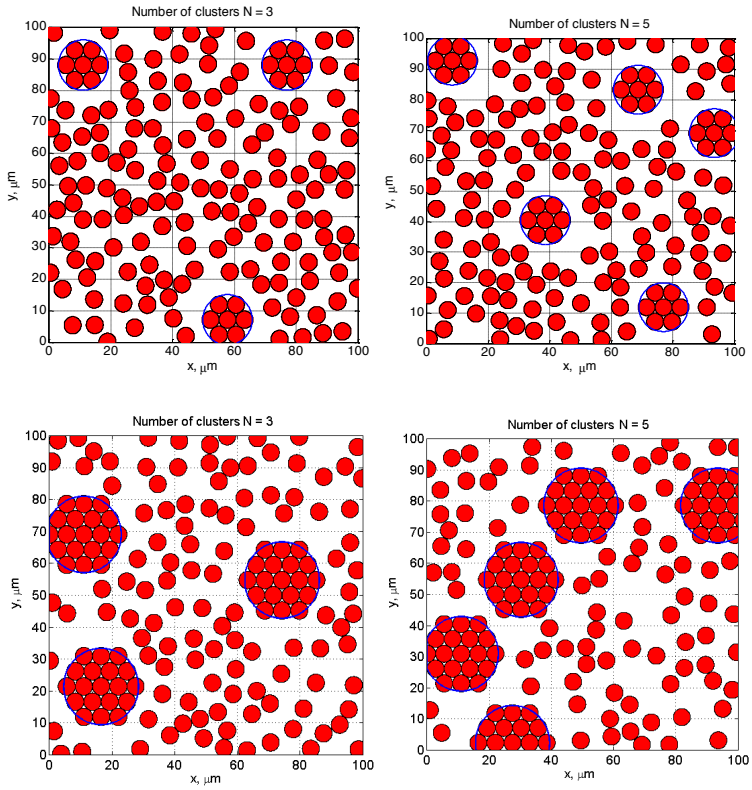


Fig. 4 Modeling of various levels of red blood cell aggregation in the blood.

4 Discussion

In Ref. [10] the authors carried out experimental measurements of an acoustic signal with OA effect in liquid solutions with carbon nanotubes. The aim of the study was to demonstrate a possibility to control of delivering nano-drugs to the required point in the body. For this purpose, an experimental setup and model solutions were developed. The authors of the study [23] calculated the profiles of OA signals and reconstructed the absorption coefficients for different wavelengths of laser irradiation. The study of biological fluids was carried out in reflection mode for OA microscopy.

The studies conducted as part of our article allow us to pre-model acoustic signals with the OA effect in various solutions, which facilitates preparation for experiments and allows us to correctly interpret the results. The obtained theoretical studies will be verified during the experiments using the LIMO 100-532/1064-U setup (Fig. 6) [21, 22]. The simulation results and subsequent experimental measurements complements to the theoretical studies carried out in Refs. [8, 11]. OA signal recording will be performed using the NI PXI 1042Q modular measuring complex, for which a block diagram of a "virtual" instrument based on LabVIEW has been developed. It is difficult to carry out experimental measurements with natural blood for several reasons, such as the difficulty of obtaining native blood, application of drugs that slow down coagulation, which will affect the measurement results. The simulated erythrocytes will be made of polymer microspheres, disks which were manufactured by Diapharm LLC (St. Petersburg) corresponding to shapes and sizes of erythrocytes, with an optical absorption coefficient close to that of erythrocytes in equivalent concentrations.

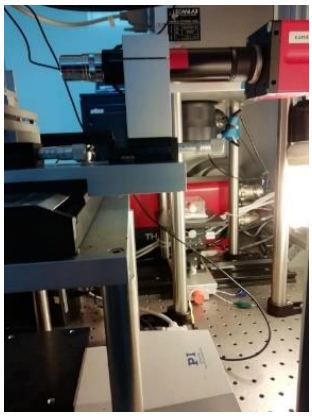


Fig. 6 Experimental setup LIMO 100-532/1064-U.

5 Conclusion

The proposed model was used to study the change in the amplitude of the acoustic signal and the spectral power density of the signal generated as a result of the OA effect, depending on the level of red blood cells aggregation and oxygen saturation. A mathematical model of red blood cell aggregation by hexagonal packing has been developed. The signals generated as a result of the OA effect from red blood cells were calculated. The possibility of recording the level of aggregation and oxygen saturation using the OA method is shown.

Disclosures

All authors declare that there is no conflict of interests in this paper.

References

1. B. G. Andryukov, A. A. Karpenko, E. V. Matosova, and I. N. Lyapun, "Raman spectroscopy as a modern diagnostic technology for study and indication of infectious agents (review)," Sovremennye Tehnologii v Medicine 11(4), 161 (2019) [in Russian].
2. M. Rui, W. Bost, E. C. Weiss, R. Lemor, and M. C. Kolios, "Photoacoustic microscopy and spectroscopy of individual red blood cells," Proceeding of Biomedical Optics and 3-D Imaging, BSuD93 (2010).
3. H. J. Meiselman, "Red blood cell aggregation: 45 Years being curious," Biorheology 46(1), 1–19 (2009).
4. J. J. Bishop, A. S. Popel, M. Intaglietta, and P. C. Johnson, "Rheological effects of red blood cell aggregation in the venous network: a review of recent studies," Biorheology IOS Press 38(2–3), 263–274 (2001).
5. S. Kim, A. S. Popel, M. Intaglietta, and P. C. Johnson, "Aggregate formation of erythrocytes in postcapillary venules," merican Journal of Physiology-Heart and Circulatory Physiology 288(2), H584–H590 (2005).
6. H. Bäumler, B. Neu, E. Donath, and H. Kiesewetter, "Basic phenomena of red blood cell rouleaux formation," Biorheology 36(5–6), 439–442 (1999).
7. A. Chabanel, M. H. Horellou, J. Conard, and M. M. Samama, "Red blood cell aggregability in patients with a history of leg vein thrombosis: Influence of post-thrombotic treatment," British Journal of Haematology 88(1), 174–179 (1994).
8. R. K. Saha, M. C. Kolios, "A simulation study on photoacoustic signals from red blood cells," The Journal of the Acoustical Society of America 129(5), 2935–2943 (2011).
9. V. V. Tuchin (Ed.), Handbook of Optical Biomedical Diagnostics, SPIE Press, PM107, Bellingham (2002).
10. G. Y. Dzhuplina, I. B. Starchenko, "System and methodology for the study of nanoscale artifacts in the bloodstream," Izvestiya SFedU. Engineering Sciences 8(10), 61–64 (2010) [in Russian].

11. I. V. Mitrofanova, I. V. Milto, I. V. Sukhodolo, and G. Y. Vasyukov, "Possibilities of biomedical application of carbon nanotubes," Byulleten' sibirskoy meditsiny 13(1), 135-144 (2014) [in Russian].
12. N. V. Sayapina, A. A. Sergievich, T. A. Batalova, M. A. Novikov, A. N. Asadcheva, V. V. Chaika, and K. S. Golokhvast, "Ecological and toxicological hazards of carbon nanotubes: a review of Russian publications," Izvestiya of the Samara Russian Academy of Sciences scientific center 16(5), 949–953 (2014) [in Russian].
13. K. A. Voronina, D. A. Kravchuk, I. B. Starchenko, D. V. and Orda-Zhigulina, "The method of express blood analysis using contrast agents – nanoparticles," In the collection: Nanotekhnologii: obrazovaniye, nauka, innovatsii, Sbornik statey X Vserossiyskoy nauchno-prakticheskoy konferentsii, 59–61 (2019) [in Russian].
14. D. A. Kravchuk, I. B. Starchenko, "Model assessment of the level of red blood cell aggregation by the optoacoustic method," Caspian Journal: Control and High Technologies 4(40), 174–183 (2017) [in Russian].
15. D. A. Kravchuk, I. B. Starchenko, "Mathematical modeling of the optoacoustic signal from red blood cells," Journal of New Medical Technologies 25(1), 96–101 (2018) [in Russian].
16. H. M. Lai, K. Young, "Theory of the pulsed optoacoustic technique," The Journal of the Acoustical Society of America 72(6), 2000–2007 (1982).
17. D. A. Kravchuk, "A mathematical model for detecting intra-erythrocyte pathologies using the optoacoustic method," Biomedical Photonics 7(3), 36–42 (2018).
18. D. A. Kravchuk, I. B. Starchenko, "Application of optoacoustic method for model calculation of non-aggregated erythrocytes and determination of hematocrit level," In the collection: Proceedings of the 2018 international conference on "Physics, mechanics of new materials and their applications", 307–316 (2019).
19. D. A. Kravchuk, I. B. Starchenko, "A theoretical model for diagnosing the effect of oxygen saturation of red blood cells using optoacoustic signals," Applied Physics 4, 89–94 (2018) [in Russian].
20. D. A. Kravchuk, "Simulation of acoustic signals with an optoacoustic effect for the detection of red blood cells of various shapes by a laser cytometer," Applied Physics 5, 93–99 (2019).
21. D. A. Kravchuk, "Experimental studies on the excitation and registration of an optoacoustic signal in a liquid," IEEE International Siberian Conference on Control and Communications (SIBCON-2019), 8729639 (2019).
22. I. B. Starchenko, D. A. Kravchuk, and I. A. Kirichenko, "An Optoacoustic Laser Cytometer Prototype," Biomedical Engineering 51(5), 308–312 (2018).
23 P. S. Grashin, A. A. Karabutov, A. A. Oraevsky, I. M. Pelivanov, and E. V. Savateeva, "Distribution of the intensity of laser radiation in strongly scattering media: Monte Carlo simulation, theoretical analysis and results of optical-acoustic measurements," Quantum Electronics 32(10), 868–874 (2002).